AN EXPERIMENTAL STUDY OF A LEADING-EDGE ALULA-INSPIRED DEVICE (LEAD) FOR MODERATE ASPECT RATIO WINGS AT LOW REYNOLDS NUMBERS.

BY

MIHARY R. ITO

THESIS

Submitted in partial fulfillment of the requirements
for the degree of Master of Science in Mechanical Engineering
in the Graduate College of the
University of Illinois at Urbana-Champaign, 2018

Urbana, Illinois

Adviser:

Assistant Professor Aimy Wissa

Abstract

Even though Unmanned Aerial Vehicles (UAVs) operating at low Reynolds numbers are becoming common, their performance and maneuverability are still greatly limited due to aerodynamic phenomena such as stall and flow separation. Birds mitigate those limitations by adapting their wings and feather shapes during flight. Equipped with a set of small feathers, known as Alula, located near the leading edge and covering 5% to 20% of the span, bird wings can sustain the lift necessary to fly at low velocities and high angles of attack. The proposed alula-inspired leading-edge device (LEAD) increases the capability of a wing to maintain higher pressure gradients by modifying the near-wall flow close to the leading-edge. It also generates tip vortices that modify the turbulence on the upper-surface of the wing, delaying flow separation. The effect of the LEAD can be compared to traditional slats or vortex generators on two-dimensional wings. For finite wings, on the other hand, the effect depends on the interaction between the LEADs tip vortices and those from the main structure. This research presents the effect on lift generation of different placements of the LEAD along the span of a moderate aspect-ratio wing. Wind tunnel experiments were conducted on a wing with an S1223 airfoil at post-stall and deep-stall angles of attack and at low Reynolds numbers of 100,000 and 135,000. To quantify the aerodynamic effect of the device, the lift generated by the wing with and without the LEAD were measured using a 6-axis force and torque transducer, and the resulting lift coefficients were compared. Results show that, in general, the location of the LEAD root yielding the highest lift enhancement was 50% semi-span away from the wing root. Lift improvements of up to 29% for post stall and 32% for deep stall were obtained at the best location, demonstrating that the three-dimensional effects of the LEAD are important. The lift enhancement was also more prominent on a finite moderate aspect-ratio wing (3D) than on an airfoil (2D), confirming that the LEAD is a three-dimensional device. Wake boundary layer sampling through hot-wire anemometry showed that stall forms at the root of the rectangular test wing and propagates toward the tip. The addition of the LEAD to the wing resulted in a reduction of velocity deficit, indicating the attenuated flow separation, in the region along the wingspan that is covered by the device. Identifying the configurations and deployment parameters that improve lift generation and mitigate stall the most is needed to design an adaptive LEAD that can be implemented on a UAV wing for increased mission-adaptability.

"Whatever you do, work heartily, as for the Lord and not for men, knowing that from the Lord you will receive the inheritance as your reward. You are serving the Lord Christ." - Colossians 3:23-24

Acknowledgments

First and foremost, I would like to thank my advisor, Prof. Aimy Wissa, for giving me the opportunity to work with her on this research. She constantly encourages me to pursue excellence and challenges me to reach my full potential. Thanks to her mentoring, I am growing more confident and competent as a scientist and an engineer. I would also like to thank my second mentor, Prof. Leo Chamorro, for investing his time to impart his expertise in fluid dynamics, experimental research, and technical writing to me. Along with Prof. Chamorro, I am thankful for the members of the Renewable Energy and Turbulent Environment Group (RE-TE-G) for sharing their wind tunnel facility with our research group. This partnership has been a crucial part for the completion of this research.

Next, I extend my gratitude to my colleagues in the Bio-Inspired Adaptive Morphology (BAM) lab. Special thanks to Chengfang Duan, my fellow BAM lab aerodynamicist. This challenging journey became more bearable because I had an awesome wind tunnel partner to bounce ideas of off and to gain insight from. To all the BAM-ers who gave their time to help me run experiments, namely Luis Urrutia, Kim Gustafson, Michael Yee, and Kevin Hart, you guys are champions, and I couldn't have done this without you. To my awesome moral supporters and colleagues that give me exposure to exciting engineering endeavors outside of wing design, Ophelia Bolmin and Oyuna Angatikna, thank you for helping me stay sane, well-fed, and well-rounded.

Last, but not least, I am grateful for the support of my friends and family. I would like to thank my parents and siblings for always supporting me through my wildest dreams and for their unconditional love. Also shout out to the Ito clan for taking me in as a part of the family and for always calling the gold out of me. My awesome husband, Benjamin, is the real MVP through this Master's journey. Having a partner to share curiosity, adventures, and drive to pursue hard things adds great value to my career and my life as a whole. Finally, the greatest for last, I thank God for guiding me through this journey. To Him be all the praise and glory!

Table of Contents

Nomenclature

α	Wing Angle of Attack (AOA)
α_{STALL}	Wing Stall AOA
α_{ZL}	Zero-Lift AOA
AR	Wing Aspect Ratio
β	LEAD AOA Relative to Wing Chord Line
γ	LEAD Tip Deflection Angle
ν	Kinematic Viscosity of Air
ρ	Density of Air
b	Wing Span
b_A	LEAD Span
c	Wing Chord
c_A	LEAD Chord
C_L	Finite Wing (3D) Lift Coefficient
C_l	Airfoil (2D) Lift Coefficient
$C_{L\alpha}$	Finite Wing (3D) Lift-Curve Slope
$C_{l\alpha}$	Airfoil (2D) Lift-Curve Slope
L_A	Alula Length
L_b	Bird Span
L_c	Alula Root to Wingtip Distance
L_w	Extended Wing Length
P_0	Static Pressure
P_{tot}	Total Pressure
Re	Reynolds number

s	Wing Semi-Span
U	Averaged Velocity in the Freestream Direction
U_∞	Freestream Velocity
x/c	Airfoil Chord Location, Normalized by the Wing Chord
y/s	Hot Wire Probe Spanwise Location, Normalized by the Wing Semi-span
y_A	LEAD Root to Wing Root Distance (%)
z/c	How Wire Probe Vertical Location, Normalized by the Wing Chord

1 Introduction

1.1 Research Motivation

While Unmanned Aerial Vehicles (UAVs) originated in military applications, their use in commercial, research, and civilian sectors has grown at an unprecedented rate over the recent years. UAVs currently operating in these applications have small characteristic lengths, operate in confined spaces, are flown close to humans, and are assigned tasks that demand high maneuverability. Therefore, mission adaptability, defined as the ability to safely and successfully complete multiple tasks (simple or complex) using the same vehicle, is an important design factor for such vehicles. In nature, mission adaptability is encountered in avian flight as birds engage in complex maneuvers such as take-off, landing, diving, gliding, perching, hovering, and more using the same flight apparatus.

Both bird wings and UAV wings with conventional airfoils operate at low Reynolds numbers [1], which is characterized by low speeds and small flight surfaces [2]. Despite this similarity, the flight envelope and maneuverability of birds far exceeds that of UAVs operating under the same flight conditions [3]. In fact, birds achieve mission-adaptability by morphing their wings and feathers during flight maneuvers [4]. For instance, bird wings are equipped with a set of small feathers near the leading edge, known as the alula, as shown in figure 1. When deployed, this feather structure enables the wing to sustain the lift necessary to fly at low velocities and high angles of attack.

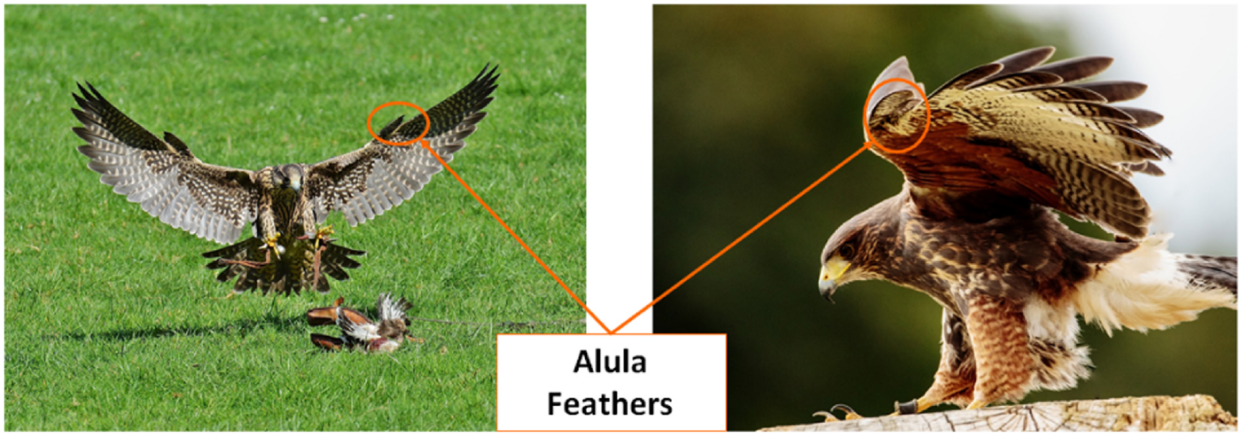

Figure 1: (Left) A falcon (photo by Alexas_Fotos/pixabay) and (Right) a yellow-billed kite (photo by Kdsphotos/pixabay) in perching maneuvers with the alula wings deployed.

The performance of UAVs, on the other hand, is greatly restricted by factors such as low weight, power limitations, and aerodynamic limitations that commonly occur under low Reynolds number conditions [3]. At low Reynolds numbers, the lift generated by a wing is

greatly reduced. According to aerodynamic principles, higher lift is obtained by increasing a lifting surface's angle of attack (AOA). However, this angle can only be increased up to the stall angle of attack, α_{STALL}, beyond which lift generation is limited by flow separation [5,6]. Therefore, alternative methods to generate high lift at low Reynolds numbers are necessary to achieve mission-adaptability in UAVs.

1.2 Research Objectives

This research proposes a Leading-Edge Alula-inpsired Device (LEAD) as a lift-enhancement and stall-mitigation device for finite wings with low to moderate aspect ratios operating at low Reynolds numbers. The effect of varying the LEAD root location along the wing span on lift generation is investigated. The performance of the LEAD on a moderate aspect ratio wing (3D) compared to the LEAD on an airfoil (2D) is quantified. Additionally, this investigation compares the effects of LEAD geometric parameters, such as the relative angle of attack with respect to the wing chord and the deflection of the LEAD tip with respect to the upper surface on the generation of aerodynamic forces. Understanding the LEAD configurations that enhance lift and mitigate stall the most is crucial to develop an adaptive design for the device.

1.3 Original Research Contributions

The following original research contributions will be developed throughout this manuscript:

- [**R.C.1**] An evaluation of the performance of a 3D rectangular wing equipped with a LEAD operating under various stall conditions (based on the wing AOA and the Reynolds numbers), confirming that the LEAD is a post-stall device in 3D flow.
- [**R.C.2**] An investigation of the effects of the placement of LEAD root along the span of the rectangular wing, confirming that the three-dimensional effects of the LEAD are important.
- [**R.C.3**] A comparison between the effects of the LEAD on the lift generated by a rectangular wing (3D) versus an airfoil (2D).
- [**R.C.4**] An evaluation of the interactions between the LEAD geometric parameters and their effects on lift enhancement.
- [**R.C.5**] A wake survey consisting of boundary layer and turbulence intensity level sampling across various span locations behind the baseline wing and the wing-LEAD assembly.

2 Background and Literature Review

2.1 Bird Wing Morphology

To achieve mission adaptability, birds adapt their wings according to flight conditions and maneuvers performed. Equipped with strong skeletal components, light muscles, and flexible feathers, wings are the most important components of the bird flight apparatus. The morphology and function of bird wings vary across species species. This section covers the internal and external structure of wings as well as the wing types encounters in various bird species.

2.1.1 Wing Structure

Internally, bird wings are supported by a modified quadruped arm skeleton as well as muscles. Structurally, these bones and muscles are both strong and light in order to meet the demands of different types of flight.

In general, a bird wing can be divided into two distinct parts: the arm wing and the hand wing (fig. 3) [7].

- The arm wing is comprised of large bones and muscles, providing mechanical support to the wing. Due to its structure, the cross-sections in this portion of the wing consist of thick airfoils with rounded leading edges, highly cambered shapes, and sharp trailing edges. Smooth adverse pressure gradients form around this region, making it suitable for low speed flight [7].

- The hand wing mostly consists of feathers, structures that are thinner and more flexible than skeletal elements. The hand wing feathers are attached and supported by small digit bones. The cross-sections throughout the arm wing are thin and slightly curved. Moreover, both the leading edge and the trailing edge are sharp. Due to its structure, this portion of the wing is well-suited for high speed flight [8].

The arm wing and the hand wing intersect at the wrist joint. The alular digit, or the thumb, is situated directly outboard of the wrist. It is covered with a set of small feathers to form the alula structure, also known as bastard wing. The joint at the root of the alula allows it to freely deflect away from the wing leading edge (forward) as well as from the wing upper surface (upward) [7].

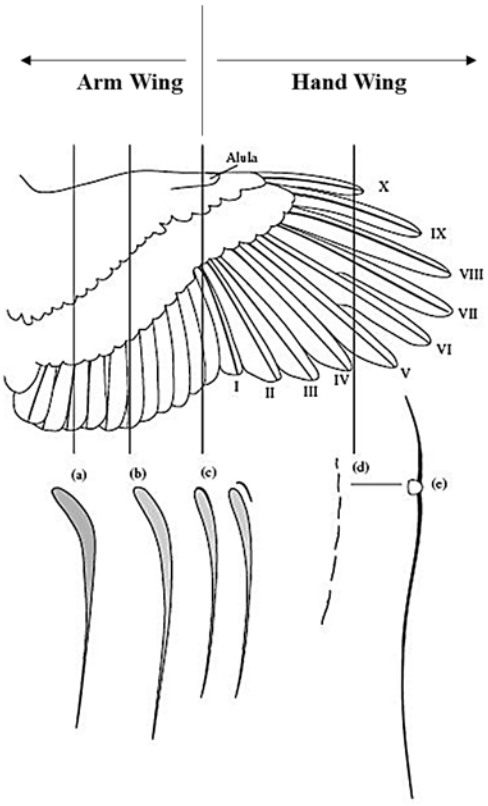

Figure 2: Schematic of a goshawk wing with cross-sections at 5 spanwise positions [a-e]. The thickest airfoil-like sections are located at the wing root and become thinner toward the tip. The alula is shown in cross-section [c]. Adapted from Videler [7].

2.1.2 Feathers of Flight

The external shape of a bird wing is determined by the feathers surrounding the internal skeletal and muscular elements. Contour feathers cover a portion of the wing and the body of the bird to create smooth and streamlined surfaces, whereas feathers of flight play important roles in generating the aerodynamic forces necessary for flight. The feathers of flight on a wing can be classified into two groups: regimes and coverts. Regimes are large and stiff feathers that support the bird during flight whereas coverts provide a streamline shape to bird wings [7]. The following groups of feathers are the most notable on a wing:

- The primary regimes consist of 9 to 11 strong feathers found in the hand wing. These feathers play an important role in thrust generation during flapping flights and are crucial to a bird's ability to fly. In many bird species, the 5 to 6 primary regimes create slots near the wing tip while the hand wing is stretched [7].

- The secondary regimes form a large portion of the surface of the arm wing as well as its sharp trailing edge. Thus, they play an important role in lift generation on a wing [7].

- The covert feathers grow in orderly rows, overlapping similarly to roof tiles, to cover the surface of bird wings. A row of greater coverts covers the implants of the primaries. A row of secondary coverts cover the implants of the secondaries [7].
- Despite the small size of the alula with respect to the rest of the wing, it is comprised of small versions of the primary regimes [7].

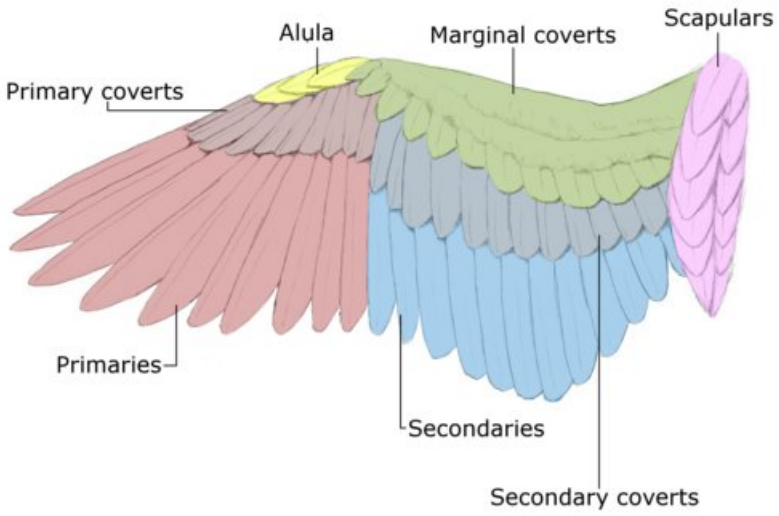

Figure 3: Schematic showing the top view of a bird wing and highlighting the different feathers of flight. The most notable feathers are the primaries and secondary regimes, the coverts, and the alula. Adapted from the Pigeon Insider.

2.1.3 Types of Bird Wings

The shape of the wing is important in determining the flight capabilities of a bird. Bird wings have been classified into four types (A, B, C, and D) based on their morphology, function, and flight performance. The following classification, also illustrated in figure 4, was adopted by Saville et al. [9]:

1. Type A, elliptical wings, are most common in birds that fly in confined environments, such as forests. Such wings can be found in *Goldfinches, Kingfishers*, and *Common Blackbirds*. The elliptical lift distribution on these wings generate smooth tip vortices. Birds with type A wings are adapted to frequent take-offs and landings and are efficient in low to moderate speeds.

2. Type B, high-speed wings, are encountered in migratory birds that fly at higher speeds and open spaces. They are encountered in species such *Doves, Kestrels*, and *Swallows*. These wings exhibit a large sweepback, low camber, and moderate to high aspect-ratios.

3. Type C, high aspect-ratio wings, are typical in birds that fly over water and long-distances without the need to frequently take-off and land. Birds that are adapted for dynamic soaring, such as *Seagulls* and *Albatrosses* are equipped with type C wings.

4. Type D, high-lift wings, and best-suited for birds of prey which fly at low speeds and frequently take-off, land, and perch. These wings typically have moderate aspect ratios with slotted wingtips. Species with type D wings, such as *Owls* and *Storks* are adapted for static soaring over land and are efficient at low speeds. The airfoils of these wings are highly cambered [10], and their alulae are more pronounced than those on other wing types.

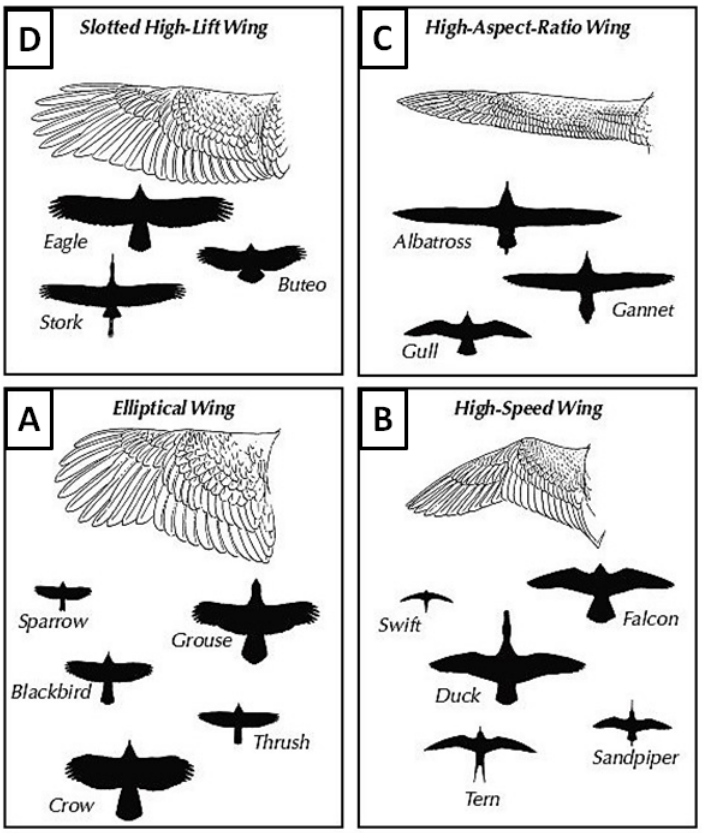

Figure 4: Bird wings are classified into 4 major types based on morphology, adaptation, and flight performance. Adapted from [11].

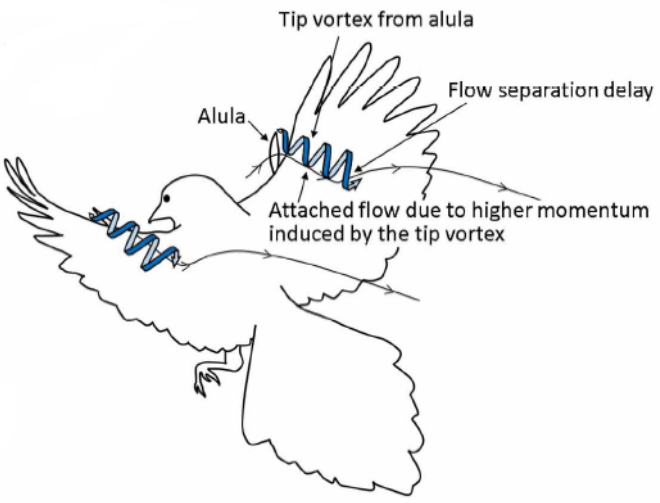

Figure 5: Artistic rendition of the effect of the alula tip vortex of the flow on the upper surface of a bird's wings. Adapted from Lee et al. [12].

2.2 The Alula in Avian Flight

2.2.1 Function of the Alula in Bird Flight

The alula feather structure is a high-lift device located near the wing leading edge on a bird. The alula, also known as bastard wing, is comprised of 2 to 6 feathers and allows the bird to fly at low speeds and high angles of attack. It is attached to the first digit bone at the root of the hand wing of the bird. In cruising conditions, it remains stowed along the upper surface of the wing near the leading-edge. During high angle of attack maneuvers, such as take-off, landing, and perching, the alula has been observed to deploy away from the wing upper surface. A number of studies have previously been conducted by biologists on the role of the alula in bird flight. Most experiments were conducted on the wing of live or dead birds with the goal understand the function of the feather structure [8, 12–14].

Lee et. al. [12] investigated the function of the alula on the aerodynamic performance of bird wings by conducting flight tasks, wind tunnel experiments, and digital particle image velocimetry (DPIV) on adult magpies. The results showed that with the alula deflected, birds performed steeper descents with great changes in body orientation during flight. Force measurements showed that when the alula is deployed, the wings generated a lift increase of 1% to 12% and a stall delay of 5° to 10°. The DPIV experiment concluded that the increase in lift is due to a streamwise vortex shed by the tip of the alula on the upper surface of the wing as shown in figure 5.

Another study on the effect of the alula in bird flight was conducted by Austin and Anderson [8] as they analyzed the wings of Redhead Ducks, Wood Ducks, Black Scoters,

and Lesser Scaups at low speeds of 7 to 20 ms^{-1} and AoAs ranging from 10° to 35°. They observed that the alula lifts away from the wing upper surface when α_{STALL} is approached. Additionally, the DPIV results obtained showed that the flow behind the wing with the alula deployed is faster and always non-reversed.

To analyze the role of the alula in bird flight from an aerodynamic point of view, Meseguer et al. [13] measured the forces generated by a pigeon wing model in a wind tunnel. This study concluded that the deflected alula causes the boundary layer to remain attached at high angles of attack and that the lift generated by the wing increased as a result.

2.2.2 Morphology of the Alula on Different Wing Types

Alvarez et al. [15] investigated the characteristics of alulae on various bird species equipped with these four types of wings listed above and compiled their results in a detailed database. The findings of this study confirmed that birds equipped with type D wings exhibit the most pronounced alulae. Table 1 shows a summary of the type D wings and alulae dimensions of the species evaluated. As recorded in table 1, the length, or span, of the alula for high lift wings ranges from 14.4% to 19.4% of the full bird span. With respect to the wing root, the alula root for a high lift wing is located between 28.6% and 41.4% semi-span away.

Table 1: Database of Type D (High-Lift) Wings as Recorded by Alvarez et al. [15]

Bird Species	**Alula Length** L_a [m]	**Wing Aspect Ratio** AR	**Alula Root to Wing Tip Distance** L_c/L_w	**Alula Length to Bird Span Ratio** $2L_a/L_b$
Bubulcus ibis	0.07	7.239	0.600	0.169
Ciconia ciconia	0.14	8.402	0.586	0.146
Milvus migrans	0.11	7.465	0.678	0.158
Gyps fulvus	0.16	6.345	0.653	0.144
Hieraaetus pennatus	0.11	7.403	0.669	0.182
Falco naumanni	0.05	8.03	0.714	0.152
Tyto alba	0.07	7.689	0.654	0.156
Otus scops	0.04	5.886	0.633	0.194
Athene noctua	0.04	5.784	0.665	0.188
Strix aluco	0.07	6.198	0.645	0.175
Average	0.09	7.004	0.649	0.166

Morphologically, the alula is located at the joint between the hand-wing and the arm-wing of birds as shown in figure 3 [7]. Therefore, the arm wing is located inboard of the alula and the hand wing outboard. Since a type D wing is well-adapted to low speed flight, its arm wing is large, and the alula is located further outboard than on wings of other types [15]. Due to these factors, birds equipped with Type D wings highly-depend on the effects of their pronounced alulae to achieve mission adaptability.

2.3 An Overview of High-lift Devices

On full-scale aircrafts, high-lift devices are components added to the wings to augment the lift generated. These devices consist of either fixed or movable structures that are actuated when needed. They are most frequently used when the aircraft is operating at speeds lower than cruising conditions such as during take-off and landing [16].

The effects of high-lift devices are obtained by modifying the chord and the camber of the airfoil of the lilting surface or by modifying the boundary layer surrounding it [17]. Devices currently in use that modify the wing's chord and camber to delay stall include trailing edge (TE) flaps [18]. Devices that modify the boundary layer surrounding the wing include vortex generators, which create vortices that energize the boundary layer over the upper surface of a wing [19]. Aircraft wings are also sometimes equipped with leading-edge (LE) slats, which modify the adverse pressure gradient on the wing's airfoil such that they are less prone to stall [20].

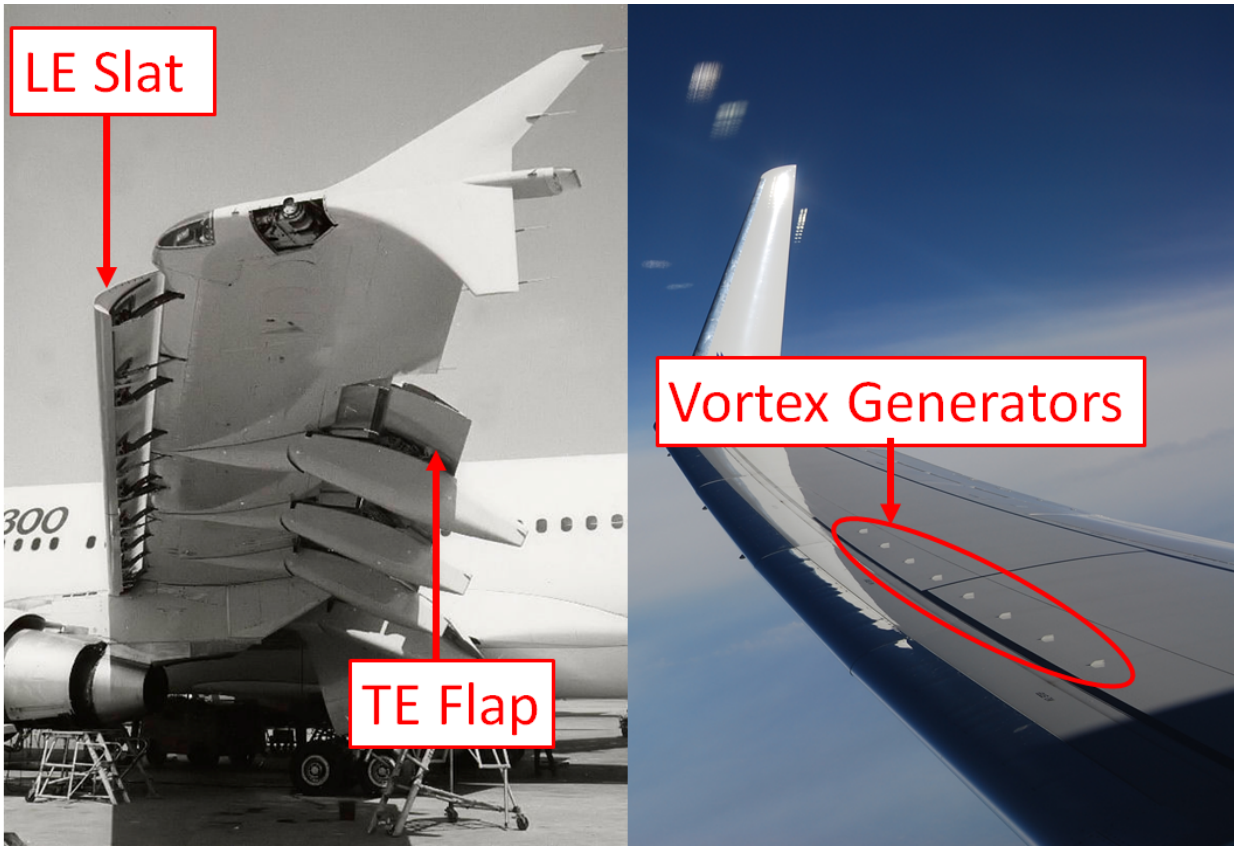

Figure 6: (Left) An airliner wing (Airbus A310-300) equipped with a trailing edge (TE) flap and a leading edge (LE) slat (photo by Adrian Pingstone). (Right) An airliner wing (Boeing 737-800) equipped with vortex generator near the leading-edge and along the span (photo by Bill Abbott).

Currently, these devices are well-suited for full-scale aircrafts; hence, they are large, heavy, and actuated by complex mechanisms. To this date, they have also been designed for aircrafts operating at high Reynolds numbers. Therefore, further investigation is necessary to design adequate high lift devices for small-scale UAVs operating in low Reynolds numbers.

2.4 Studies of Alula-Inspired Devices in Engineering (2D)

While the role of the alula in avian flight has been investigated by many researchers, the first implementation of an engineered alula device (LEAD) for lift enhancement and stall mitigation can only be found in an experimental study conducted by the members of the Bio-Inspired Adaptive Morpholgy (BAM) lab at the University of Iliinois Urbana-Champaign. The alula device was placed at the leading edge of a cambered airfoil at low Reynolds numbers [21, 22]. By collecting aerodynamic force measurements, conducting hot-wire anemometry, and visualizing the flow through 2D particle image velocimetry (PIV), Mandadzhiev et al. were able to quantify the effects of the device on the airfoil.

The results of this study have shown that the LEAD affects the airflow in two main ways. First, it modifies the boundary layer near the airfoil leading-edge to increase its capacity airfoil to sustain higher pressure gradients. This effect is also known as the slat effect. Second, the alula generates a tip-vortex that produces a streamwise flow on the upper surface of the wing. This tip-vortex effect adds momentum to the flow and delays flow separation at steep angles of attack. In this experimental study, Mandadzhiev et al. also defined two important parameters that affect the performance of the engineered alula. The alula relative angle of attack with respect to the airfoil chord was varied to modulate the strength of the tip vortex shed by the device, whereas the alula tip deflection was varied to modulate the distance between the vortex and the airfoil upper surface. The cambered airfoil equipped with the LEAD as presented by Mandadzhiev et al. [22] produces more lift and is subjected to a flow separation delay at high angles of attack.

Since the alula is typically found on birds with low and moderate aspect-ratios, a 2D experiment gives an insightful but incomplete picture of the effects of the LEAD on a lifting surface. Therefore, as outlined in the research objectives in 1.2. Thus, an experiment on a 3D wing with and without the LEAD is necessary to further understand the aerodynamic effects of the device.

3 Methodology

3.1 Aerodynamic Experimental Setup

Systematic wind-tunnel experiments were performed to characterize the aerodynamic effects of the LEAD on a moderate aspect ratio wing at high angles of attack. These measurements were taken at low Reynolds numbers for a baseline configuration and for wing equipped with a LEAD. The experiments conducted consisted of the following:

- Force/torque measurements to quantify the aerodynamic forces generated by the wing with and without the LEAD.
- Hot-wire anemometry to characterize the behavior of the flow in the wake of the wing and LEAD assembly.

3.1.1 Wind Tunnel

All experiments for this research were conducted in an closed section, open-loop, constant pressure wind tunnel in the Renewable Energy and Turbulent Environment lab at the University of Illinois Urbana-Champaign. The wind tunnel has four test sections of equal length and cross-sections. The first section, which is closest to the inlet, was chosen for the experiment because the flow is nearly uniform, the boundary layer is the thinnest, and the turbulence level is as low at 0.1% at this location. The wind tunnel cross-section is rectangular with a height of 0.45m and a width of 0.9m.

A pitot-static tube was placed 5 airfoil chords ahead of the wing leading-edge to set the test section flow velocity. The static and total pressure signals were collected using a differential pressure transducer in order to obtain a dynamic pressure reading. The differential signal was processed and output by an analog port on the National Instrument cDAQ-9133. To obtain flow velocity, the dynamic pressure was converted based on Bernouilli's equation as shown in equation 1.

$$V_\infty = \sqrt{\frac{2(P_{tot} - P_0)}{\rho}} \tag{1}$$

3.1.2 Force/Torque Instrumentation

To quantify the aerodynamic forces generated, the wing-LEAD assembly described in 3.2 was firmly mounted to an ATI Industrial Automation Gamma 6-axis force transducer. This instrument has a high signal-to-noise ratio, a sensitivity of 1/160 N (0.006 25 N, and a

saturation levels of 35 N of force per axis channel and 2.5 Nm torque per torque channel. Calibration was supplied by the manufacturer at 1% of the full measurement scale for each force axis.

The force transducer was then attached to a stepper motor-based precision rotary table such that the airfoil was free to rotate about its aerodynamic center (quarter chord location). This device was controlled using a computer through a micro-controller board to output percise and repeatable wing AOAs. The entire force/torque test apparatus was in turn mounted to the side wall of the wind tunnel as shown as figure 7 such that the sensor X-axis and the wing chord are aligned with the airflow when the AOA is zero. The force and torque readings were collected using the NI cDAQ-9133 controller and the NI 9205 analog input module.

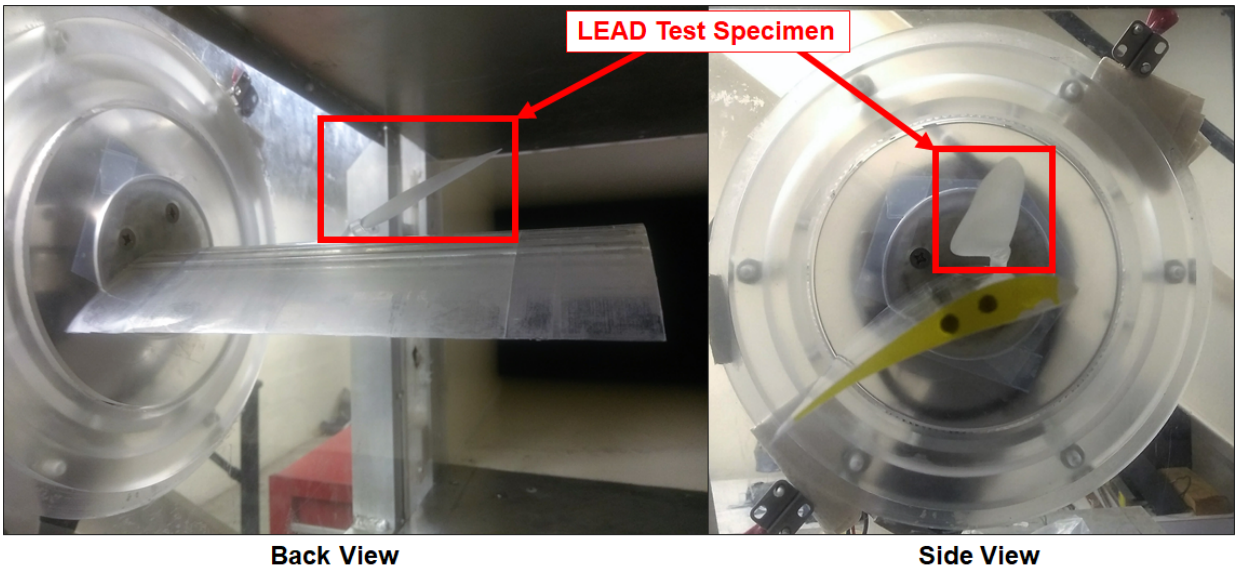

Figure 7: Wind Tunnel Experiment Setup of Rectangular Wing with s1223 Airfoil Cross-Section Equipped with LEAD Specimen.

3.1.3 Hot-Wire Anemometry

To observe the behavior of the flow in the wake, the boundary layer was sampled using a hot-wire probe placed at at $x/c = 1.125$ behind the trailing edge of the base wing as shown is figures 8 and 9. The anemometer is made with a 5.0 μm tungsten wire, and connected to a DANTEC Dynamic data-collection system. To ensure repeatability, the hot-wire probe was positioned using a traversing system that allowed it to move upward and spanwise at fixed intervals.

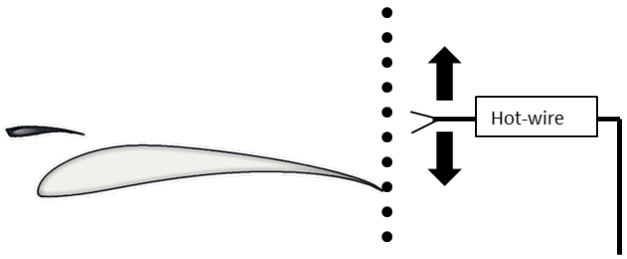

(a) The hot-wire probe was placed at $x/c = 1.125$ behind the trailing edge of the base wing and moved upward to sample the boundary layer.

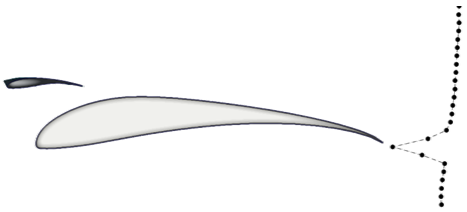

(b) Example of velocity deficit profile expected from hot-wire experiment on airfoil schematic.

Figure 8: Experimental setup and configuration for hot-wire anemometry.

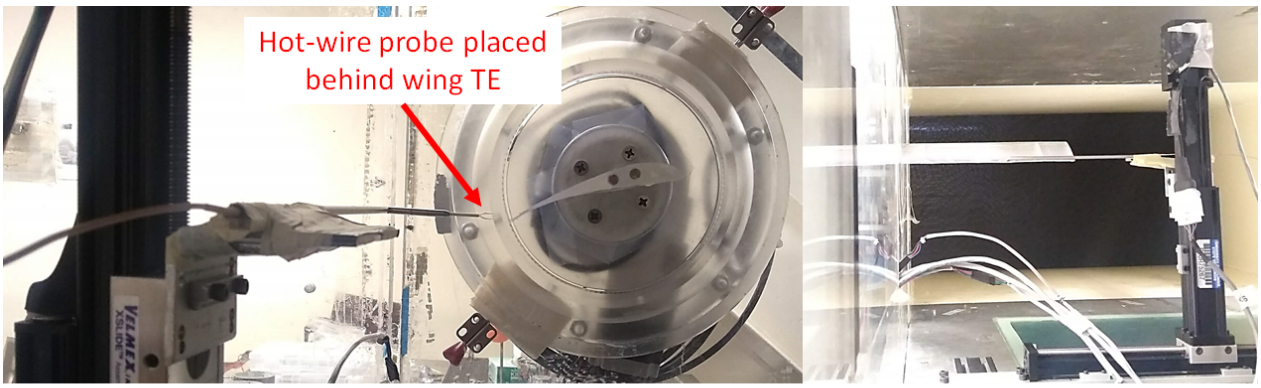

Figure 9: Experimental setup of hot-wire anemometry

3.2 Wing and LEAD Test Specimens

3.2.1 Wing Test Specimen

To achieve similar aerodynamic effects as the wing shapes and alula morphological parameters observed in the bird species discussed previously (table 1), the semi-span (distance from wing root to tip, $b/2$) for the test specimen was set to 220mm, the chord (c) to 80mm. Therefore, the aspect ratio (AR) obtained was moderate at 5.5. The selected airfoil for this wing was the S1223, which has a maximum thickness of 12.1% at 19.8% of the chord and a maximum camber of 8.1% at 49% of the chord. This high-lift and highly cambered airfoil is similar to typical type D wing profiles [10, 23].

A solid model of the rectangular wing was created, then it was manufactured from cured photo-polymer resin using the Forms 2 by FormLabs stereolithography (SLA) printer. To obtain precise and reliable LEAD root locations along the span of the wing (y_A), quick-connect slots that are compatible with the LEAD connector described in 3.2.2 were created

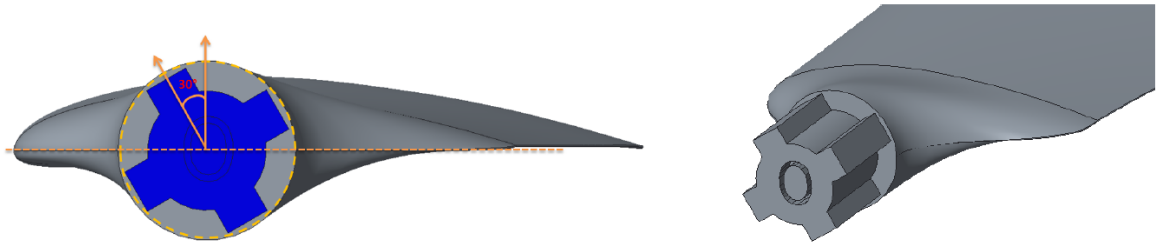

(a) Alula angle of attack, β is controlled by a key locking mechanism.

(b) Isometric view of the interlocking features.

Figure 10: Model of keyed mechanism controlling the relative LEAD angle of attack β.

on the upper surface, along the leading edge. Figure 11 illustrates the design and dimensions of the rectangular wing.

3.2.2 LEAD Test Specimen

The LEAD test specimen covered 15% of the wing span (30% of the semi-span, with a mean chord (c_a) of 18.7mm and a span (b_A) of 67.5mm. A model of the rectangular wing equipped with the LEAD are shown in figure 11. The airfoil selected for the specimen, the NACA22 (12% maximum thickness at 24.2% chord and 68% maximum camber of at 54.1% chord), is commonly used in leading-edge devices. The LEAD has an elliptical chord distribution along the span and exhibits a soft stall behavior.

Furthermore, the tip of the LEAD specimen was deflected at an angle γ with respect to the wing upper surface. Precise and repeatable values for this geometric parameter were obtained by designing a LEAD connector for each angle measured as shown in figure... The connector's locking mechanism is compatible with the slots along the wing leading-edge to ensure that it stays fixed at the desired location. The LEAD chord offset by an angle of attack relative to the main wing's chord, β. This angle was obtained by designing the LEAD with a plus-shaped keyed mechanism as shown in figure 10 . They key feature was compatible with the LEAD connector and allowed the specimen to stay at a fixed angle during test runs.

The airfoil, the LEAD relative angle of attack (β), and the tip deflection angle (γ) are defined in figure 12 and their values were varied as summarized in 3.3. The LEAD specimens used in were modeled and manufactured similarly to the rectangular wing specimen.

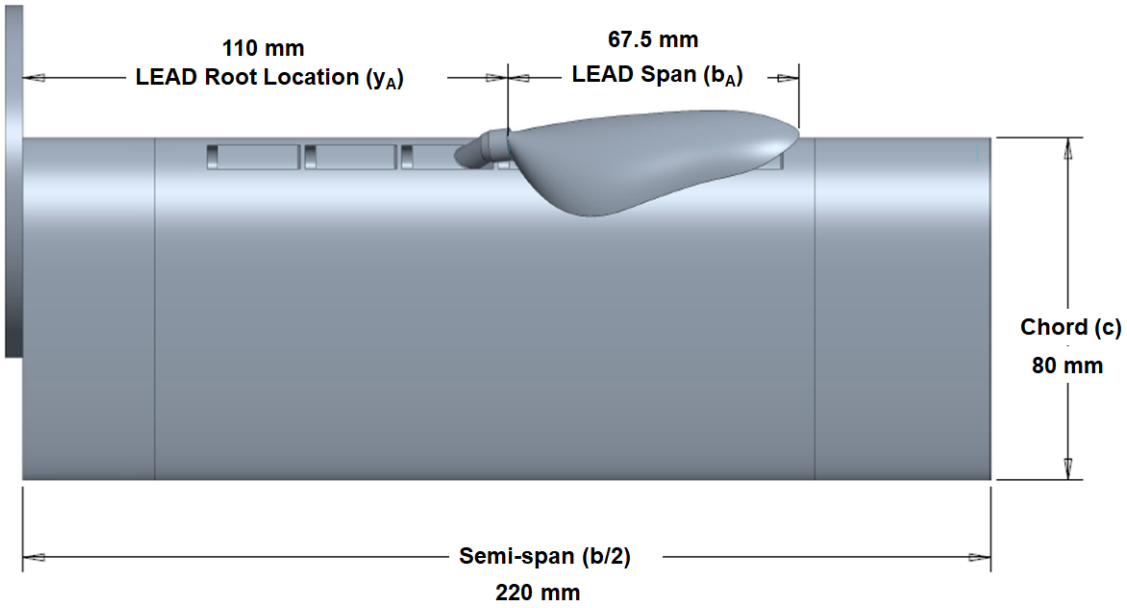

Figure 11: Model of rectangular test wing equipped with LEAD specimen showing the LEAD root at the $y_A = 50\%$ location.

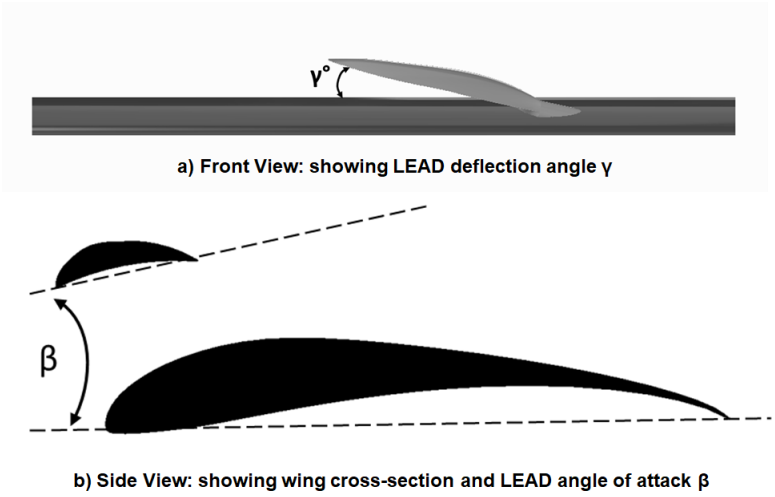

Figure 12: Illustration of the wing-LEAD assembly showing the tested geometric parameters β and γ. Adapted from Mandadzhiev et al. [22].

3.3 Experiment Matrix

3.3.1 Force/Torque Measurements

The wind speed in the wind tunnel was varied to produce low Reynolds numbers of 100,000 and 135,000. To obtain the baseline lift coefficients, the wing angle of attack, α, was varied in increments of 1° from -10° to 30° for Re = 100,000 and from -10° to 40° for Re = 135,000. For the wing equipped with the LEAD, the angles of attack (α) evaluated were 10°, 18°, 26°. For Re = 135,000 $\alpha = 34°$ was added in order to capture the behavior of the wing at deep stall conditions.

The following LEAD geometric parameters were tested:

- AOA relative to wing chord: β = -18°, -13°, -10°, -5° (β = -28° and -13° were added to the experiment matrix for the Re = 135,000 $\alpha = 34°$, whereas $\beta = 5°$ and 10° were omitted)
- LEAD tip deflection: γ = , 4°, 13°, 22°
- Distance from wing root to LEAD root, as a percentage of the semi-span ($s = b/2$): y_A/s = 30%, 40%, 50%, 60%, 70%

3.3.2 Hot-Wire Measurements

The flow and geometric parameters that resulted in the greatest improvements in lift were then evaluated in wake surveying method through hot-wire anemometry. Table 2 shows the the configurations for which these measurements were taken.

Table 2: Hot-Wire Experiment Matrix Based on Configurations that Resulted in the Greatest Lift Enhancement

Reynolds number **Re**	**Wing AOA** α	**LEAD Relative AOA** β	**LEAD Tip Deflection** γ	**LEAD Root Location** y_A
100,000	18	-5	22	40
100,000	26	-13	22	50
135,000	26	-5	22	60
135,000	34	-13	22	50

As discussed in section 3.1.3, the hot-wire probe was placed at $x/c = 1.125$ behind the trailing edge of the base wing. To sample the boundary layer a selected spanwise location, it was moved upward from $z/c = -0.2$ (below the TE) to $z/c = 0.6$ (above the TE in increments of 5mm. As far as the spanwise location was concerned, the following key locations were chosen: in-board of the LEAD, at the LEAD root, mid-span of the LEAD, at the tip of the

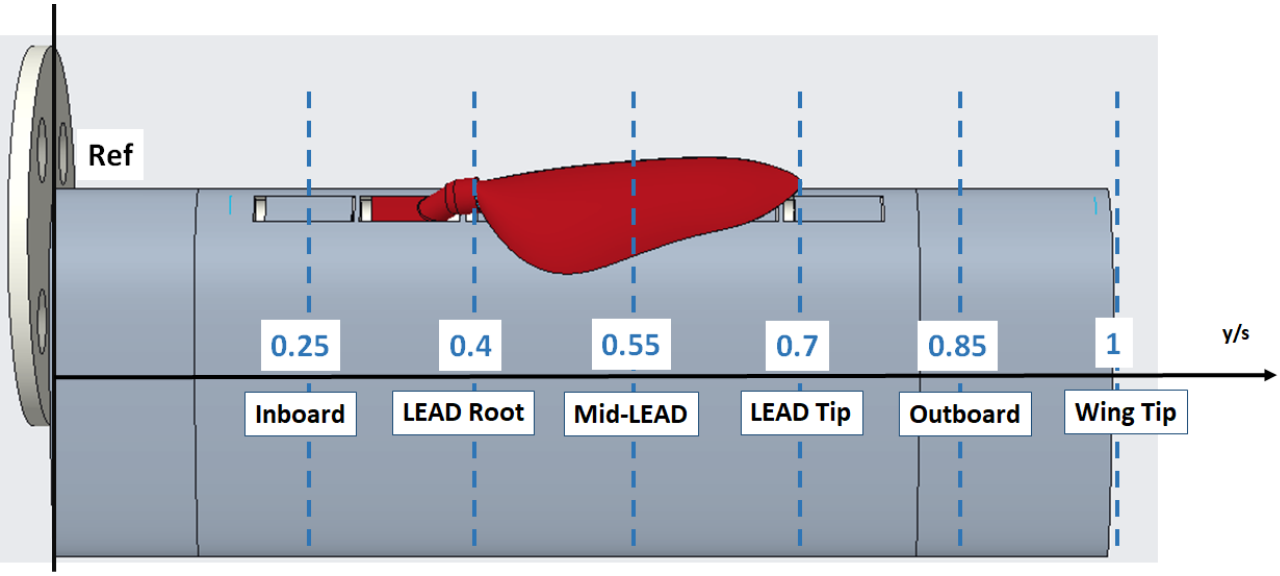

Figure 13: Boundary layer sampling was performed at key locations on the wing for both baseline and wing-LEAD assembly setups.

LEAD, outboard of the LEAD, and at the wingtip. Figure 13 illustrates the span placement of hot-wire probe during a test run.

4 Results and Discussion

4.1 Force/Torque Results

The wing evaluated in this experiment is finite (3D) with a moderate aspect ratio; therefore, three-dimensional corrections were applied to the linear region of the airfoil (2D) C_l vs. α curves to obtain a 3D lift curve slope, $C_{L\alpha}$. The lift-curve slope generated by a 3D wing as a function of a 2D lift-curve slope depends on the aspect ratio and is given by equation 2 [2]. Furthermore, two wings with the same airfoil cross-section share a common zero-lift angle of attack, α_{ZL} [2]. Thus, the lift curves for the 2D and the 3D wings should cross at the coordinates $\alpha = \alpha_{ZL}$ and $C_L = 0$.

$$C_{L\alpha} = C_{l\alpha}\frac{AR}{(AR+2)} \tag{2}$$

The baseline lift coefficients C_L obtained at each angle of attack are shown in figure 14 for Re = 100,000 and in figure 15 for Re = 135,000. These plots also indicate the validation of the experimental 3D data obtained against the s1223 airfoil C_l vs. α curves that are published in literature [24]. The linear region of each curve matches up with the theoretical lift-curve slope computed based on equation 2, and the two curves cross at α_{ZL} = -5.36°.

Figure 16 shows the baseline coefficients used to compute the percent differences in lift due to the LEAD. Each angle of attack of at which the rectangular wing was equipped with the LEAD is marked. Based on the trends observed in the C_L vs. α curves obtained, the angles of attack were classified into three stall conditions as shown in table 3. For the rest of this manuscript, these stall terms will be used to characterize the angles of attack.

Table 3: Angle of Attack Classifications

Re	α **= 10**	α **= 18**	α **= 26**	α **= 34**
100,000	Pre-stall	Post-stall	Deep Stall	N/A
135,000	Pre-stall	Pre-stall	Post-stall	Deep stall

4.1.1 LEAD is Post-stall Device on a 3D Wing

Figure 17 indicates the effects of the LEAD on a three-dimensional wing at each angle of attack α and each Reynolds numbers tested. The percent difference between the lift coefficient generated by the wing-LEAD assembly and the baseline was computed and plotted against the wing angle of attack. The figure contains main effects plots (%C_L vs. α); therefore, the contribution of only one parameter, α, is presented while the contribution of

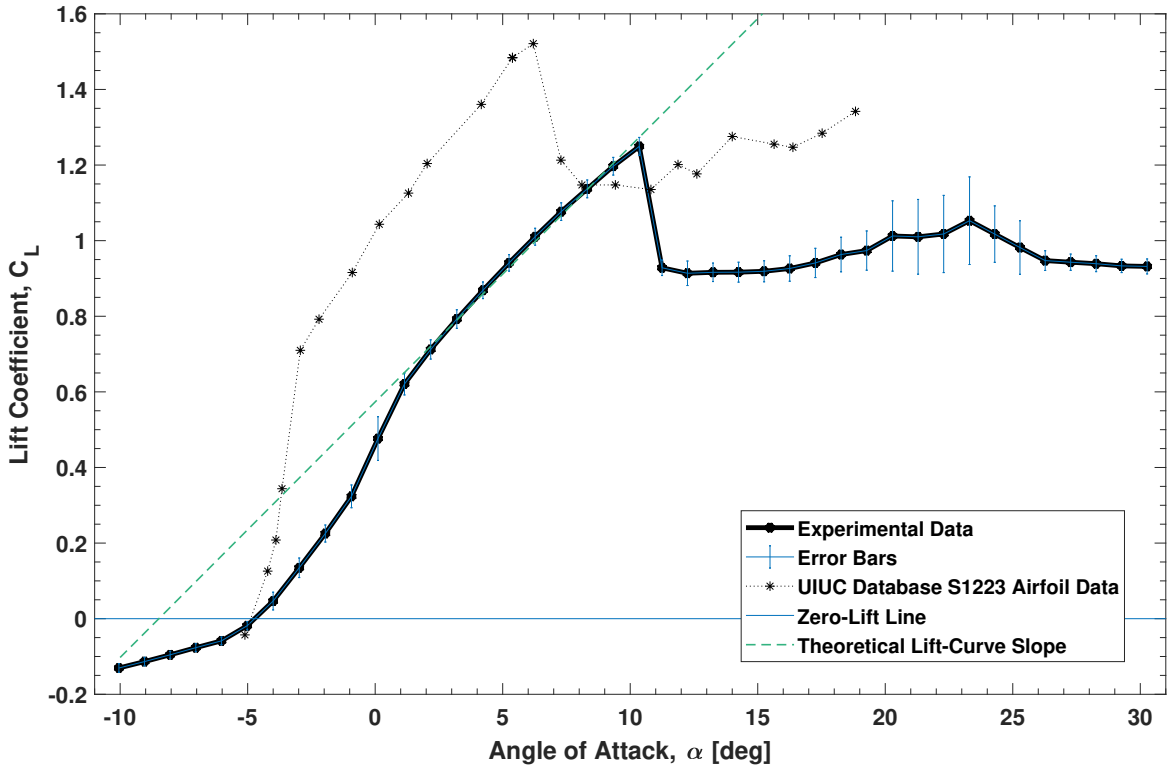

Figure 14: Validation of 3D experimental results at Re = 100,000 against the s1223 airfoil data published by Selig et al. in [24].

all other geometric parameters (β, γ, and y_A/s) is averaged. Overall, the LEAD deteriorated the performance in pre-stall conditions. Once the angle of attack of the wing was set to post stall, the wing equipped with the LEAD generated on average 1.5% more lift than the baseline at Re = 100,000 (where $\alpha = 18°$ at post-stall) and 12.9% at Re = 135,000 (where post-stall $\alpha = 26°$). Greater improvements were obtained when the wing was under deep stall conditions. On average, the LEAD enhanced the lift coefficient by 8.4% at Re = 100,000 (Deep stall $\alpha = 26°$) and 11.8% at Re = 135,000 ($\alpha = 34°$). These results agree with the previous experiment conducted by the Mandadzhiev et al. [21,22], confirming that the LEAD is also a post-stall device when placed on the leading-edge of a 3D wing.

4.1.2 Effects of LEAD Spanwise Placement on Lift

In this section, the results from the post-stall and deep stall angles of attack are analyzed at each Reynolds number in order to understand the effects of the LEAD root location on lift generation. Figure 18 shows the percent change in lift coefficient, between the baseline wing and the wing equipped with the LEAD, plotted against the LEAD angle of attack (β) and

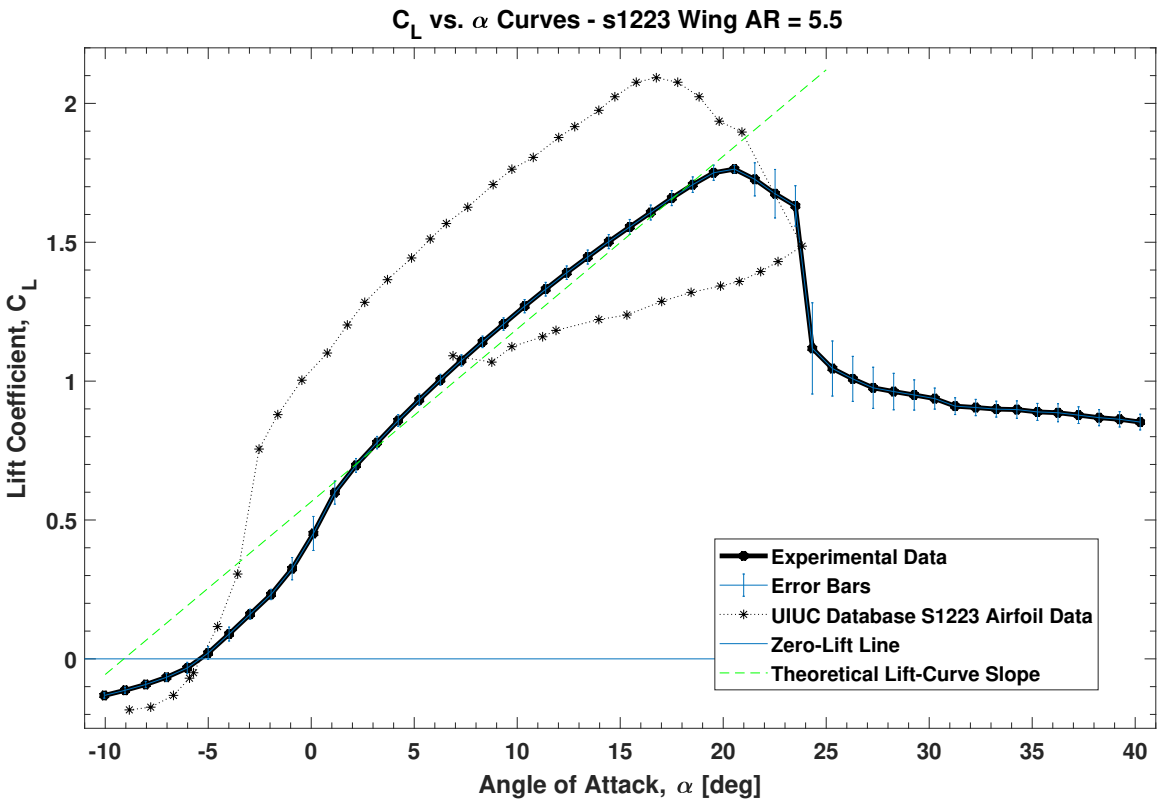

Figure 15: Validation of 3D experimental results at Re = 135,000 against the s1223 airfoil data published by Selig et al. in [24].

deflection (γ) at Re = 100,000. The plots shown are main effect plots; thus, the contribution of only one geometric parameter is presented while the second parameter is averaged (e.g. the top plots show $\%C_L$ vs. β with averaged γ values at different locations y_a/s). These results indicate that the LEAD increased the lift generated by the wing at post-stall (α = 18°) and deep stall (α = 26°) angles of attack. At Re = 100,000, the greatest increase in lift due to the LEAD was up to 32%, occurring when the wing is in deep stall (α = 26°). This greatest increase was obtained when the LEAD root was placed 50% semi-span away from the wing root. Once the device was moved outboard of this location, however, the lift enhancement declined but still remained favorable. Once the LEAD has reached the most outboard location (70% semi-span away from the wing root), the LEAD tip protruded outboard of the wing tip, and all configurations generated lift coefficients lower than the baseline. For all locations, a LEAD relative angle of attack of β = -5° resulted in the greatest lift enhancement at post-stall, whereas β = -13° performed best in deep stall. Furthermore, under all stall conditions and at all locations, a tip deflection of γ = 22° consistently yielded the highest increase in lift coefficient at most angles of attack.

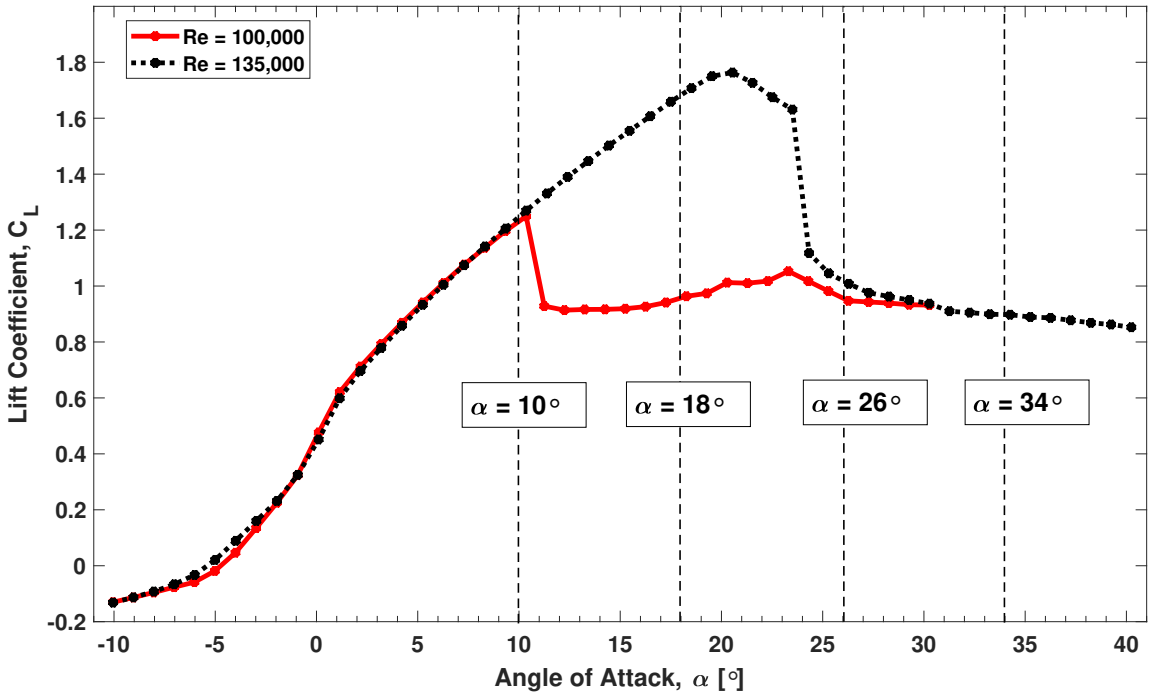

Figure 16: Experimental results showing the lift coefficient generated by the 3D rectangular wing at Re = 100,000 and Re = 135,000. The wing-LEAD assembly was tested at each angle of attack α marked.

The performance for the same geometric parameters at Re = 135,000 is shown in figure 19. In this case, the wing stall angle α_{STALL} increased from 10° to 20°. As a result, α = 18° became a pre-stall angle of attack, so α = 26° was categorized as post-stall and α = 34° as deep-stall. The results obtained were similar to Re = 100,000, except the location yielding the best performance was y_A/s = 60% in the post-stall condition. Additionally, the greatest increase in lift, up to 29%, produced by the LEAD occurs when the wing is in post-stall. Similarly to Re = 100,000 results, lift enhancements declined as the LEAD was moved outboard of the location of highest improvement. Furthermore, a tip deflection of γ = 22° and relative angle of attack of β = -13° consistently increased the lift coefficient the most at all locations and angles of attack.

4.1.3 LEAD is Three-Dimensional Device

To evaluate the LEAD as a three-dimensional device, the improvements in lift coefficient obtained at the location (y_A/s) yielding the highest increased were compared to the results obtained in the airfoil configuration as tested by Mandadzhiev et al. in [21] for a given Reynolds number and stall conditions (α). The results shown in figure 20 indicate that the

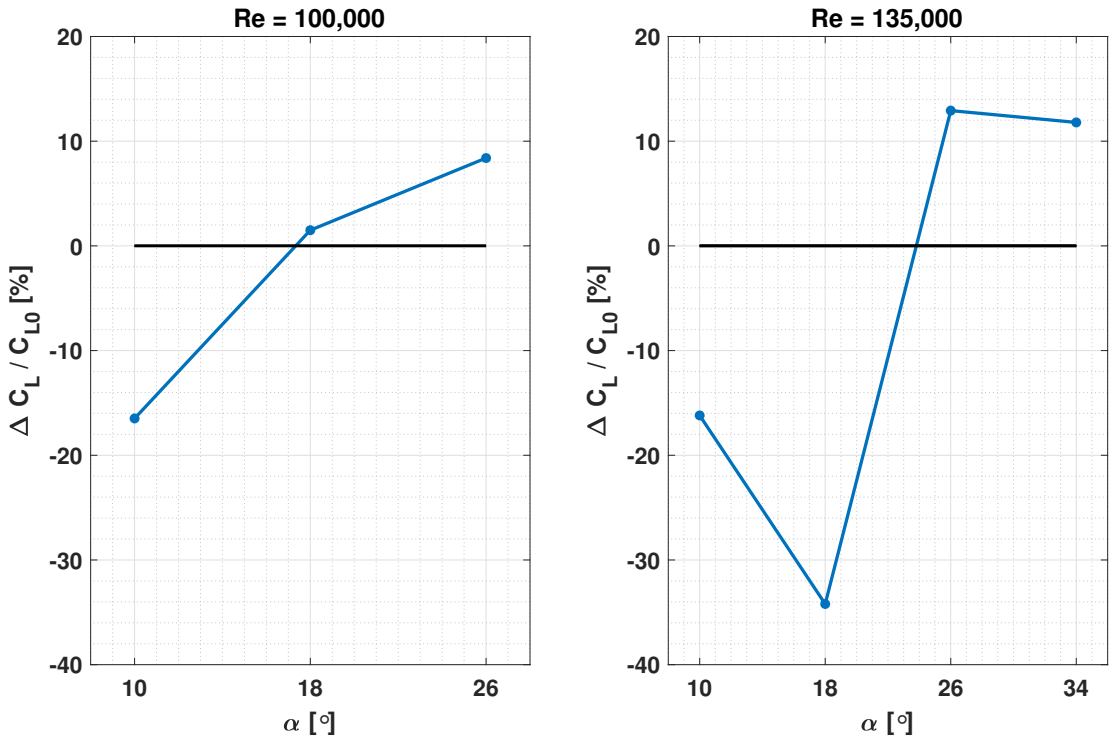

Figure 17: Main effects of wing angle of attack, α, on the percent difference between the lift generated by the wing equipped with the LEAD and the baseline wing. The effects of the following geometric parameters are averaged: β, γ and LEAD root location.

device enhanced the lift coefficient generated by the wing for both cases (2D and 3D). However, the finite wing (3D) with a LEAD generated a higher percent lift difference compared to its airfoil (2D) counterpart.

At $Re = 100{,}000$, the LEAD on an airfoil yielded C_l improvements ranging from 1% to 5% in both post-stall and deep stall conditions. While the LEAD on a finite wing improved the lift coefficient within ranges similar to the airfoil configuration under post-stall conditions, the results show that it enhanced C_L significantly more with a range of 9% to 32% under deep stall conditions.

At $Re = 135{,}000$, the airfoil configuration yielded a higher increase in lift, ranging from 11% to 22% in post-stall compared to $Re = 100{,}000$. The finite wing configuration, on the other hand, generated an increase of 11% to 29%. Overall, the results show higher lift enhancement when the LEAD is placed on a finite wing as opposed to an airfoil.

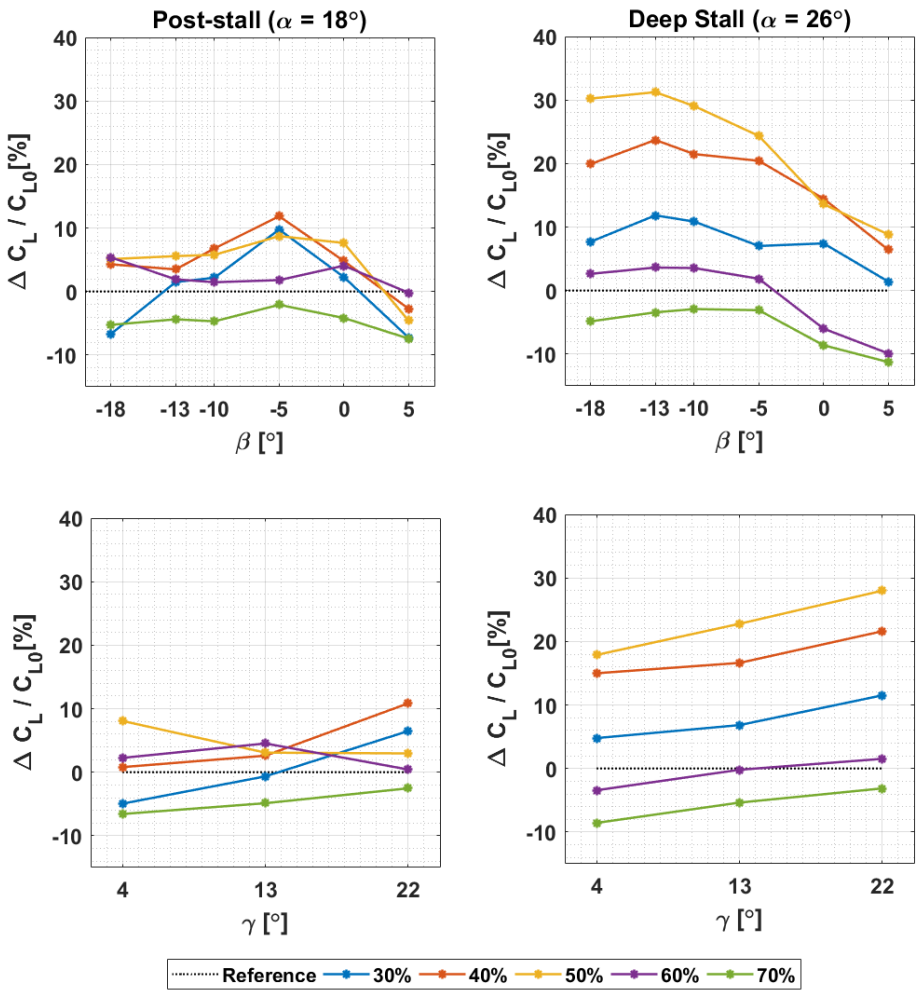

Figure 18: Percent difference in lift coefficients generated by the baseline wing and the wing-LEAD assembly (Main Effects) at Re = 100,000. Each curve represents the results at each root location. (Top) Main effects of β with averaged γ. (Bottom) Main effects of γ with averaged β.

4.1.4 Effects of LEAD Geometric Parameters on Lift

Figure 21 shows interaction plots between the geometric parameters of LEAD at post-stall and deep stall angles of attack at Re = 100,000. Therefore, the contribution from each value of β and γ is evaluated in order to observe any effects they have on one another. The results shown were obtained at the locations that produced the highest lift enhancement (40% semi-span for post-stall and 50% for deep stall). Even though the majority of the relative angles of angles β evaluated produced a percent change in lift coefficient, the general trend of the plots show that the lower angles yielded the best performance. This occurs especially in the deep stall conditions. As far as the tip deflection angle, γ in concerned, higher angles

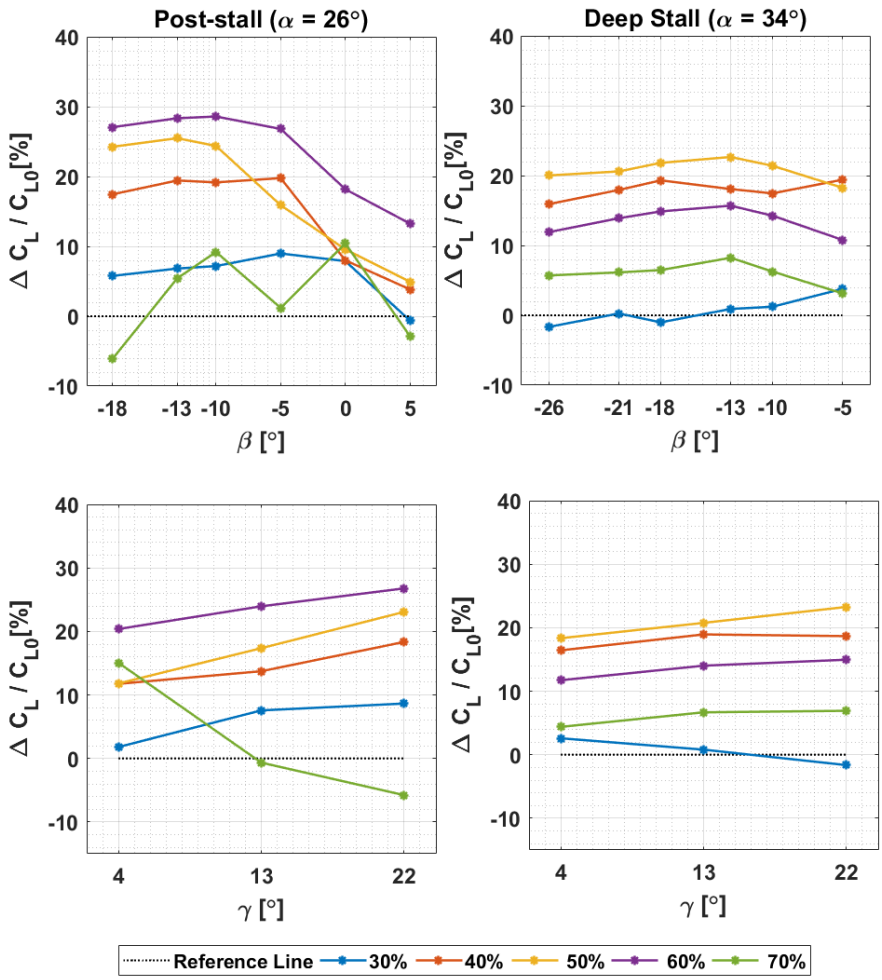

Figure 19: Percent difference in lift coefficients generated by the baseline wing and the wing-LEAD assembly (Main Effects) at Re = 135,000. Each curve represents the results at each root location. (Top) Main effects of β with averaged γ. (Bottom) Main effects of γ with averaged β.

constantly yield greater lift enhancement. The same trends were observed for Re = 135,000 as shown in figure 22.

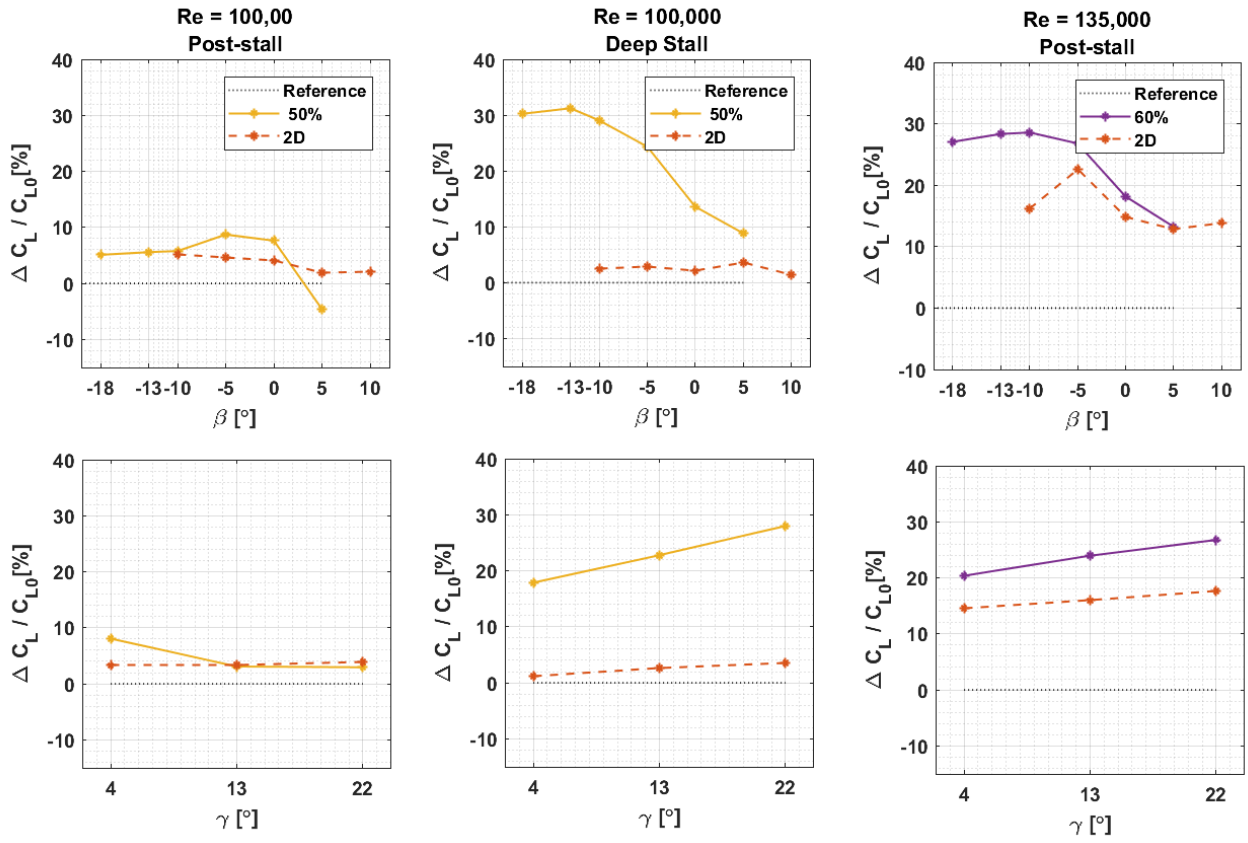

Figure 20: Comparison between lift percent differences generated by a LEAD on a wing (3D) and a LEAD on an airfoil (2D). Each curve represents the results at each root location. (Top) Main effects of β with averaged γ. (Bottom) Main effects of γ with averaged β.

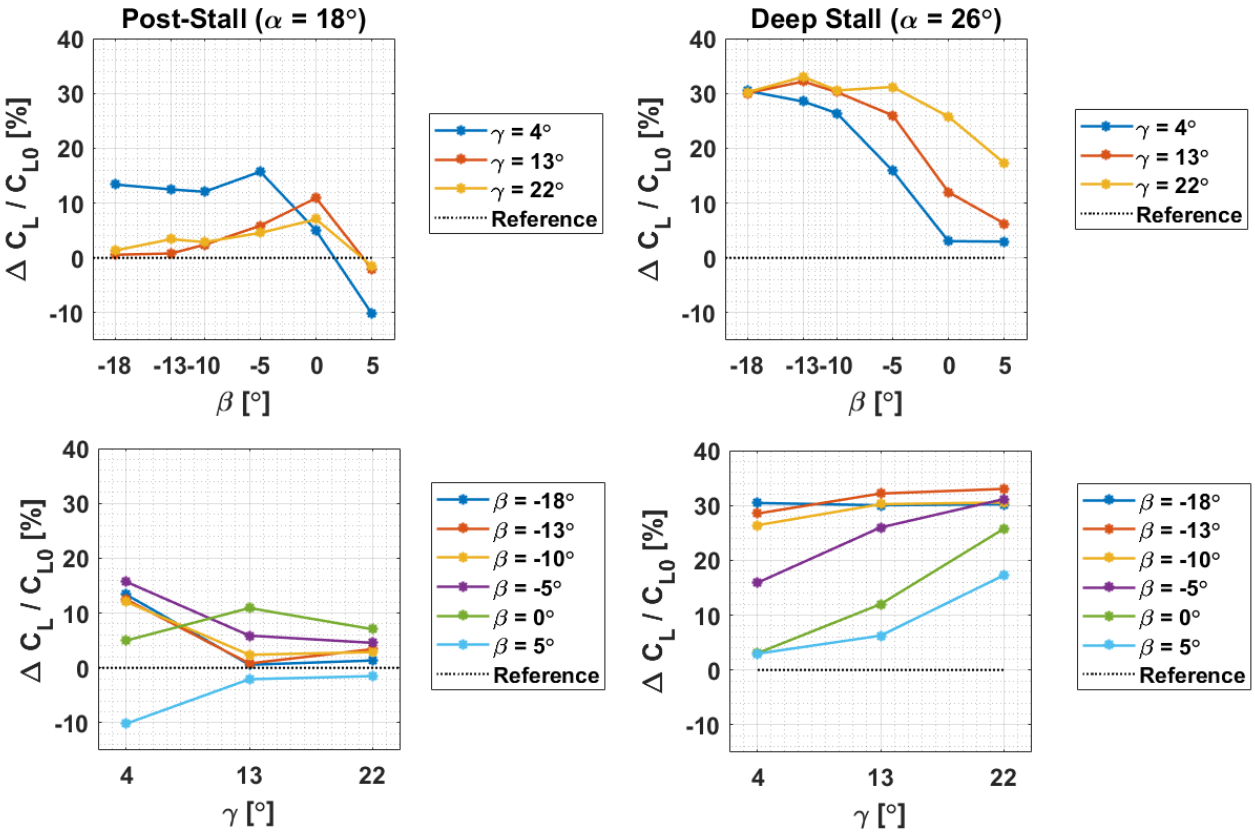

Figure 21: Interaction of β and γ in the percent difference in lift coefficients generated by the baseline wing and the wing-LEAD assembly at Re = 100,000. (Left) Post-stall plots at 40% Location. (Right) Deep stall plots at 50% Location.

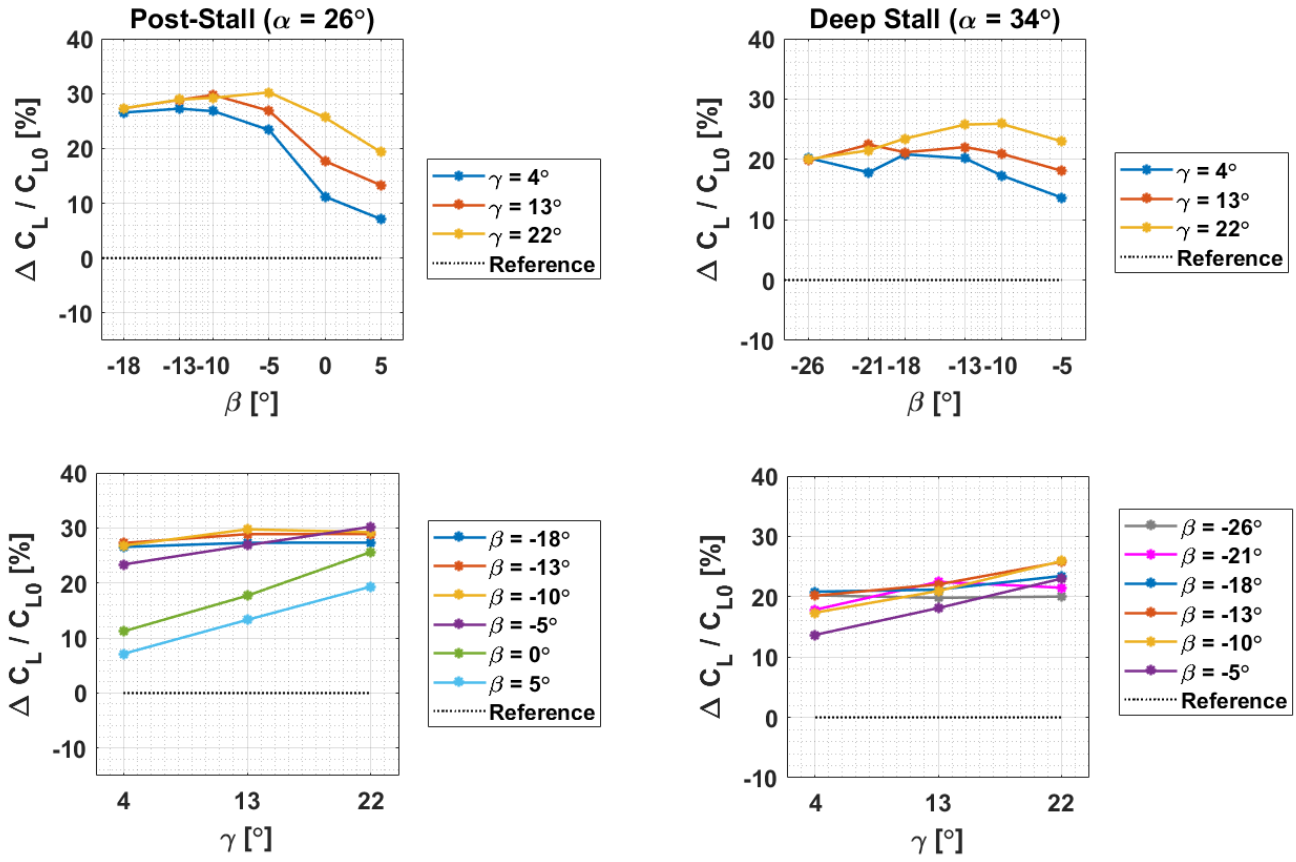

Figure 22: Interaction of β and γ in the percent difference in lift coefficients generated by the baseline wing and the wing-LEAD assembly at Re = 135,000. (Left) Post-stall plots at 50% Location. (Right) Deep stall plots at 60% Location.

The combination between the geometric parameters β, γ, and y_A/s that generated the highest lift are then presented in figures 23 and 24. These plots show a surface on which the percent improvement in lift is of equal value. Therefore, all configurations enclosed within the cone plotted in the two figures yield a lift increase that is greater than the iso-level value indicated. E.g., in order to obtain a lift coefficient change above 32% in the deep stall condition at Re = 100,000, the ideal geometric parameters for the LEAD should be chosen from: -13.5° < β < -11.5°, 15° < γ < 25°, and 48.5% < y_A/s < 50%.

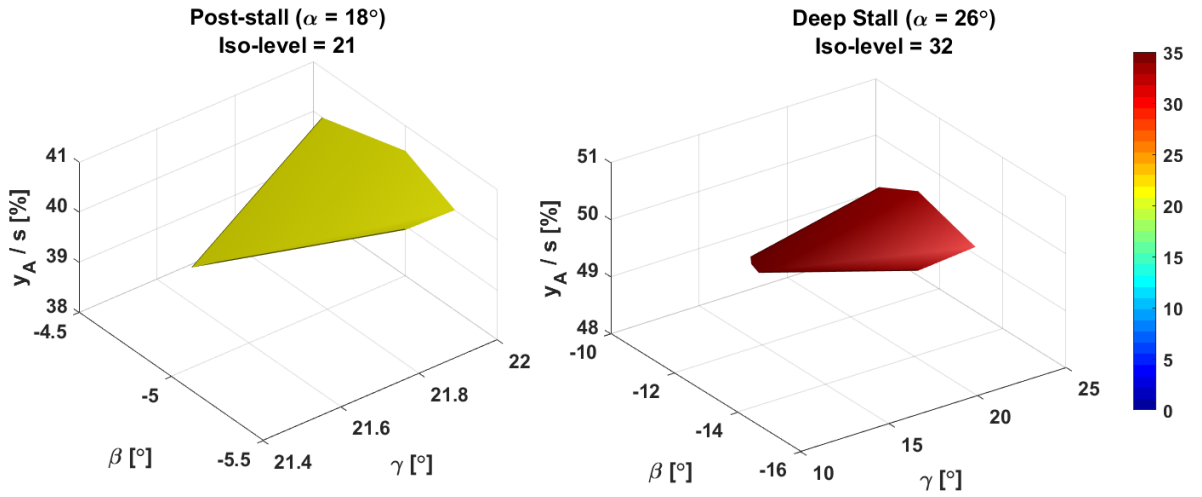

Figure 23: Isosurfaces at Re = 100,000 showing a conical surface enclosing the percent improvement in lift greater or equal to indicated iso-level.

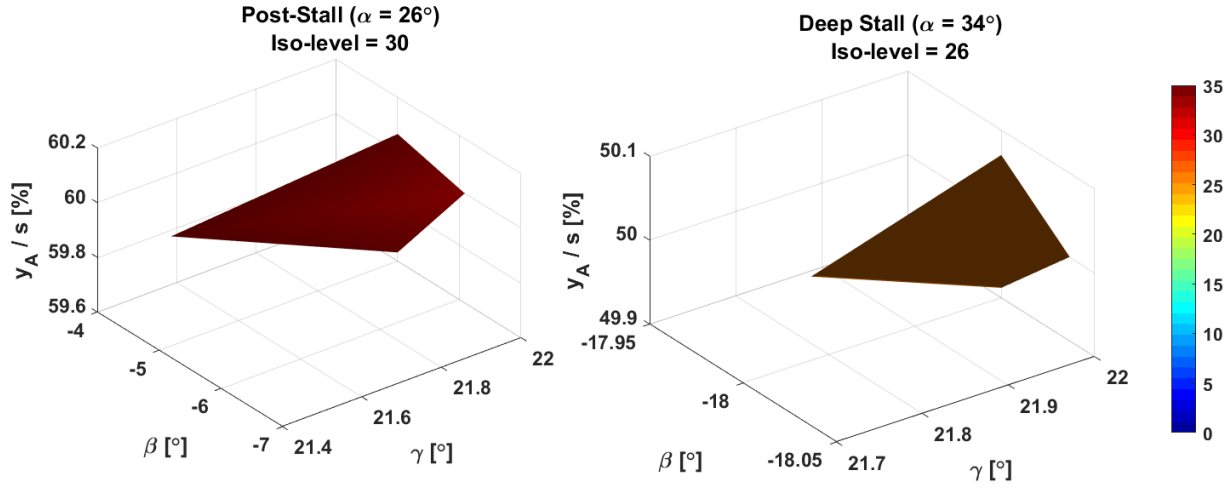

Figure 24: Isosurfaces at Re = 135,000 showing a conical surface enclosing the percent improvement in lift greater or equal to indicated iso-level.

4.2 Hot-Wire Results

By placing the hot-wire probe described in 3.1.3 at various locations along the wing span (y/s) and at $x/c = 1.125$ (10mm behind the wing trailing edge), the effect of the LEAD on the wake was characterized. For that, the wake velocity deficit profile and the turbulence intensity level generated were plotted for each spanwise location at post-stall and deep stall conditions. Figure 25 shows the post-stall wake deficit profiles obtained behind the trailing edge of the baseline wing at Re = 100,000, whereas figure 26 displays the ones obtained at a deep stall angle of attack and at the same Reynolds number. Under both conditions, the velocity deficit profiles show that the largest separation region at the location that is closest to the wing root ($y/s = 0.25$ for post-stall and $y/s = 0.35$ for deep stall). As the hot-wire probe was moved outboard, the wake profiles show progressively smaller velocity deficits. At the wing tip ($y/s = 1$), a full recovery to the freestream velocity, hence no separation, was observed.

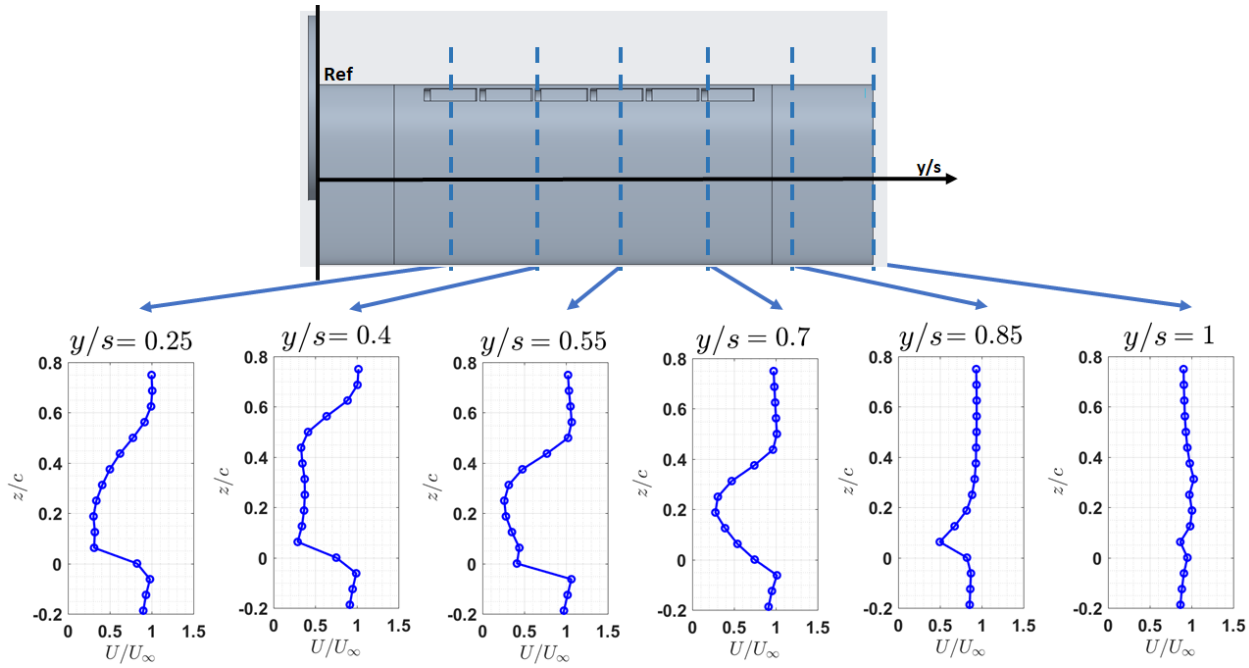

Figure 25: The velocity deficit profiles (mean velocity over time normalized by the freestream velocity, starting from 0.2c below incrementing toward 0.8c above the wing upper surface) was evaluated at various locations behind the baseline wing at post stall conditions ($\alpha = 18°$) at Re = 100,000. Stall starts at the wing root and propagates toward the tip.

Similarly, figures 27 and 28 show the post-stall and deep stall wake profiles respectively at Re = 135,000. At this Reynolds number, the velocity deficit follows the same trends across the wing span as the results obtained at Re = 100,000. However, while the wake velocity was fully recovered to the freestream near the wing tip at post-stall conditions, a

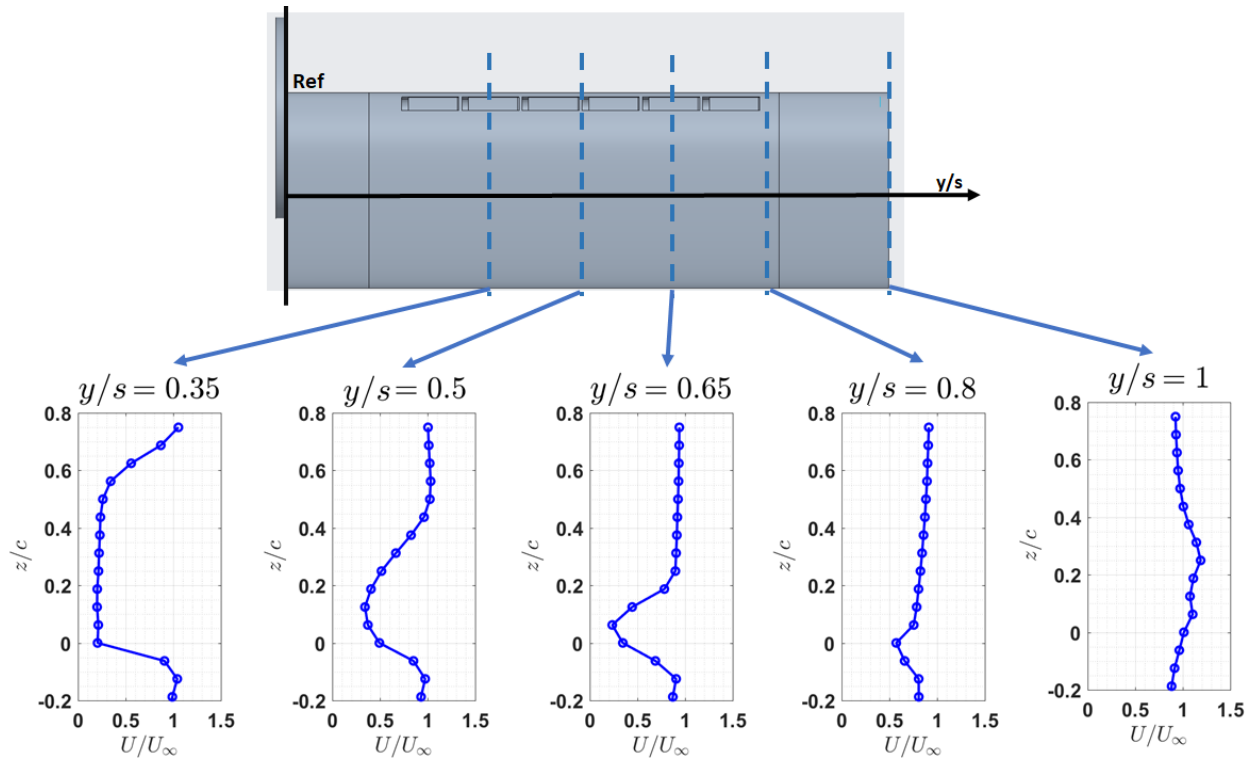

Figure 26: The velocity deficit profiles (mean velocity over time normalized by the freestream velocity, starting from 0.2c below incrementing toward 0.8c above the wing upper surface) was evaluated at various locations behind the baseline wing at deep stall conditions (α = 26°) at Re = 100,000. Stall starts at the wing root and propagates toward the tip.

large velocity deficit was observed at this location when the wing was in deep stall. This indicates flow separation across the entire wing span at this angle of attack ($\alpha = 34°$) and Reynolds number (Re = 135,000).

These baseline results are in agreement with the fact that, in rectangular wings found conventional aircrafts, stall and flow separation start at the root and propagate outboard toward the tip [2].

4.2.1 LEAD Effects on Boundary Layer: Velocity Profiles and Turbulence Intensity

In this section, the wake velocity profiles obtained from the rectangular wing equipped with the LEAD are compared to the baseline results. Figure 29 compares the velocity deficit profiles at a post-stall angle of attack at Re = 100,000. The results show a positive effect of the LEAD, which is characterized by a reduction in wake deficit at $y/s = 0.55$ (mid-span of the LEAD). Additionally, the largest turbulence intensity levels measured was shifted downward, closer to the wing upper surface, at this location, as shown in figure 29. This

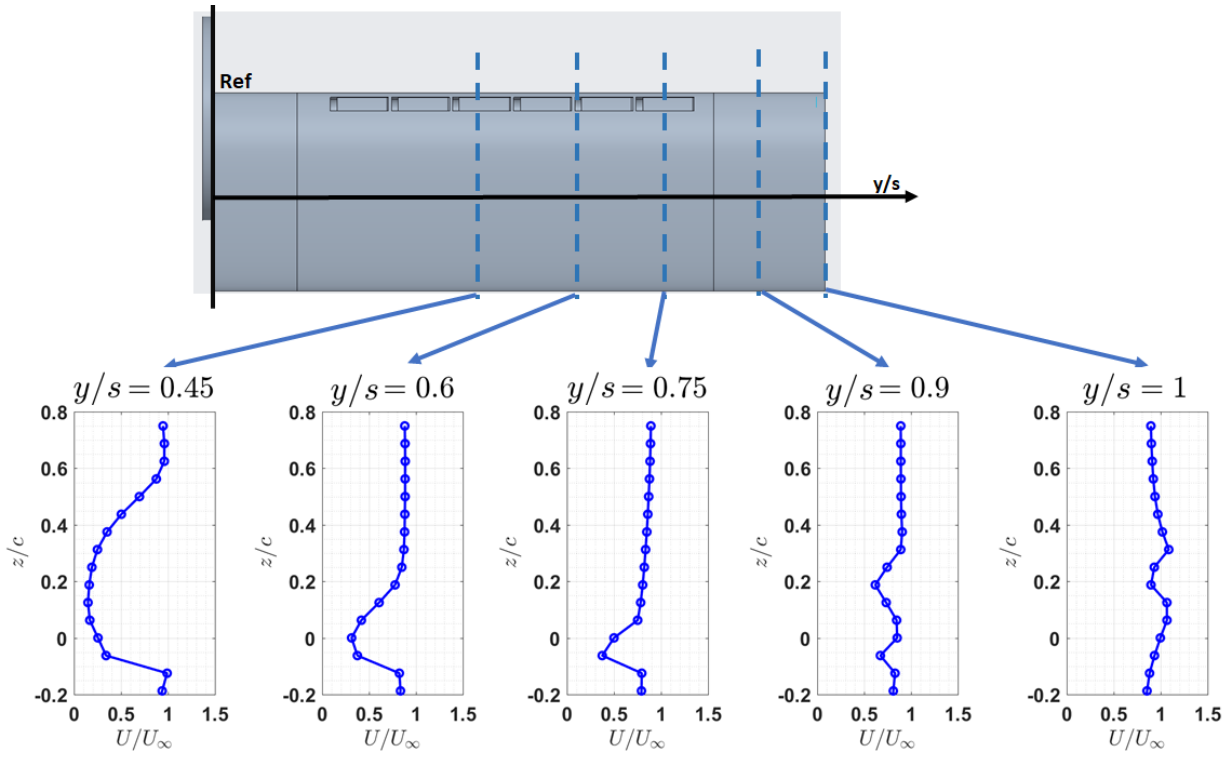

Figure 27: The velocity deficit profiles (mean velocity over time normalized by the freestream velocity, starting from 0.2c below incrementing toward 0.8c above the wing upper surface) was evaluated at various locations behind the baseline wing at post stall conditions ($\alpha = 26°$) at Re = 135,000. Stall starts at the wing root and propagates toward the tip.

shift indicates a thinner and more energetic shear layer between the free stream and the highly mixed flow in the wake. No significant effects on the velocity deficit profiles were obtained inboard and outboard of the LEAD.

Trends similar to the results obtained under post stall conditions were observed in the boundary layer profiles under deep stall conditions at Re = 100,000. Figure 30 show a slight reduction in the velocity deficit at $y/s = 0.65$, which also corresponds to the location at the mid-span of the LEAD. However, a greater velocity deficit can be observed at the LEAD root at $y/s = 0.5$. No significant effects on the velocity deficit profiles were observed inboard and outboard of the LEAD.

Figure 31 shows the same comparisons described above for Re = 135,000 at a post-stall angle of attack. The velocity profile inboard of the LEAD root under these flow conditions exhibit no alterations compared to the baseline. At the root of the LEAD, a greater separation is observed in the wake of the wing equipped with the LEAD compared to baseline. However, the velocity profiles obtained at all spanwise locations outboard of $y/s = 0.75$ (mid-LEAD) show reduced deficits and full recovery to free stream.

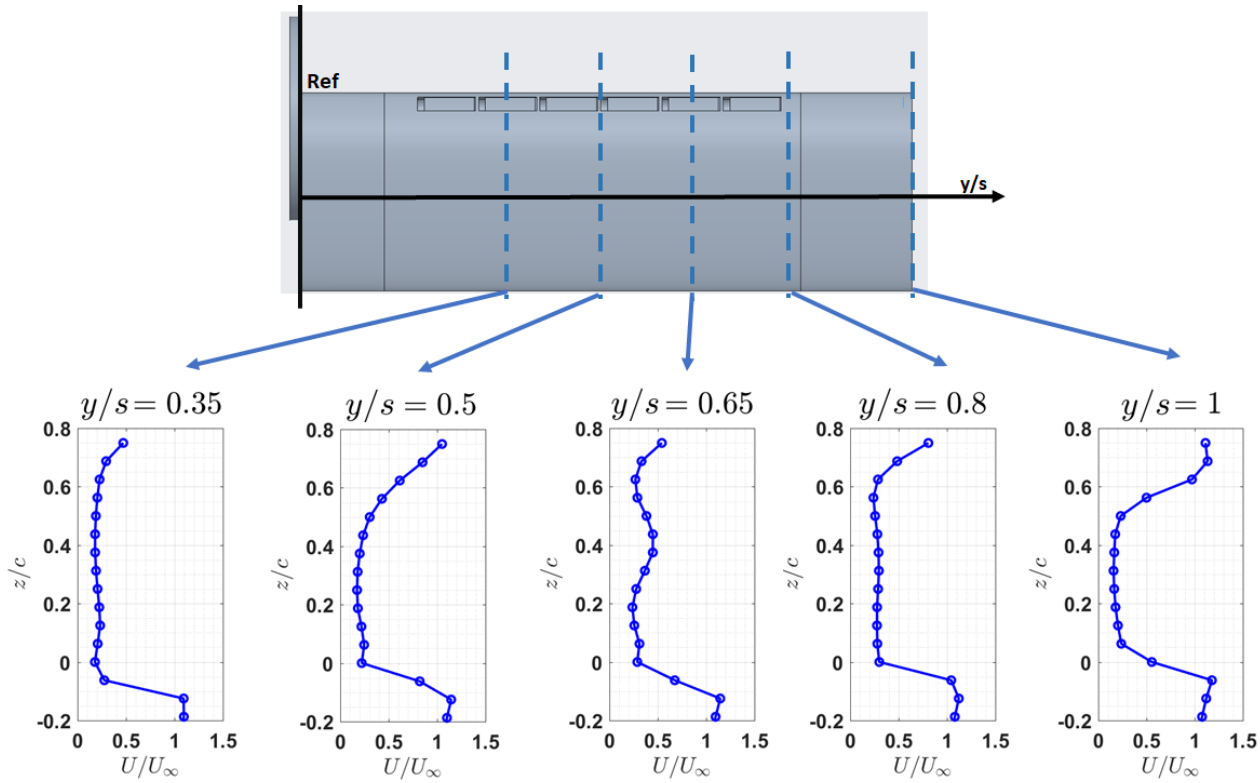

Figure 28: The velocity deficit profiles (mean velocity over time normalized by the freestream velocity, starting from 0.2c below incrementing toward 0.8c above the wing upper surface) was evaluated at various locations behind the baseline wing at deep stall conditions ($\alpha = 34°$) at Re = 135,000. Stall starts at the wing root and propagates toward the tip. At this angle of attack, stall is observed across all span locations

Lastly, the wake velocity profiles obtained under deep stall conditions at Re = 135,000 follow similar trends as the ones observed in post stall at the same Reynolds number. The LEAD-wing assembly produced a profile similar to the baseline inboard of the LEAD root. At $y/s = 0.5$, the LEAD root location, the wake behind the assembly also shows a slightly larger separation compared to the base wing. The greatest reduction in velocity deficit are observed outboard of the LEAD under these conditions. At $y/s = 0.8$ and $y/s = 1$, while the wake produced by the baseline was separated, the addition of the LEAD on the upper surface of the wing greatly alleviated. At the wingtip, the flow velocity has been recovered to freestream.

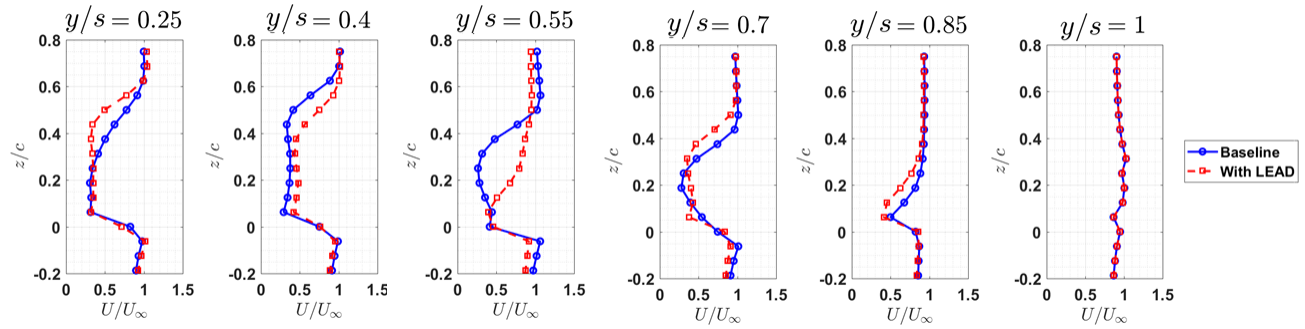

(a) Velocity Deficit Profiles. The mean velocity over time were evaluated and normalized by the freestream velocity at each spanwise location starting from 0.2c below to 0.8c above the wing upper surface.

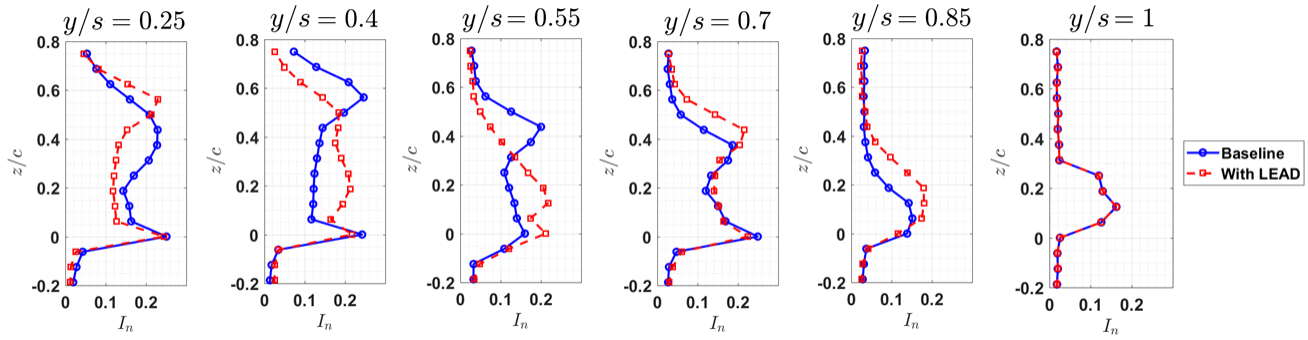

(b) Turbulence Intensity Levels. The velocity fluctuations over time (standard deviation) were evaluated at each spanwise location starting from 0.2c below to 0.8c above the wing upper surface.

Figure 29: Boundary layer sampling results under Post Stall conditions (α = 18°) at Re = 100,000. The LEAD root was fixed at the 40% location. The LEAD parameters were fixed at β = -13° and γ = 22°.

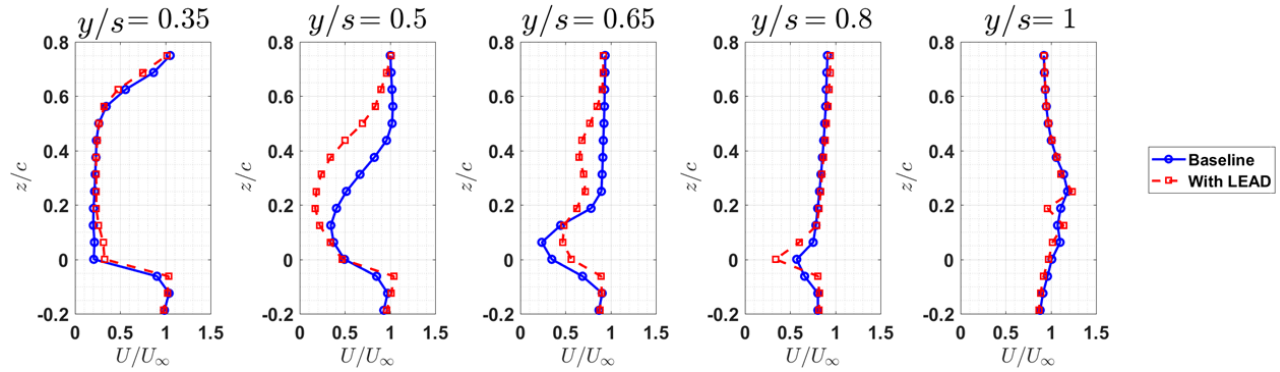

(a) Velocity Deficit Profiles. The mean velocity over time were evaluated and normalized by the freestream velocity at each spanwise location starting from 0.2c below to 0.8c above the wing upper surface.

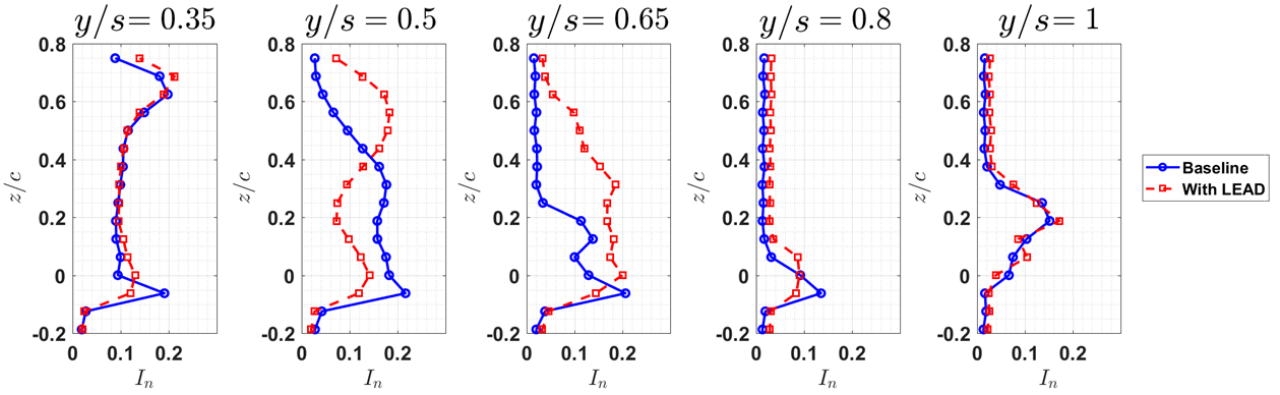

(b) Turbulence Intensity Levels. The velocity fluctuations over time (standard deviation) were evaluated at each spanwise location starting from 0.2c below to 0.8c above the wing upper surface.

Figure 30: Boundary layer sampling results under Deep Stall conditions (α = 26°) at Re = 100,000. The LEAD root was fixed at the 50% location. The LEAD parameters were fixed at β = -13° and γ = 22°.

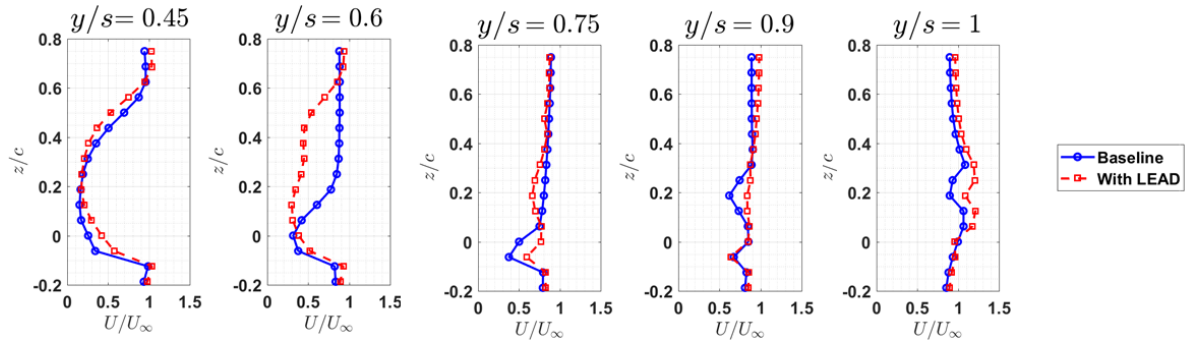

(a) Velocity Deficit Profiles. The mean velocity over time were evaluated and normalized by the freestream velocity at each spanwise location starting from 0.2c below to 0.8c above the wing upper surface.

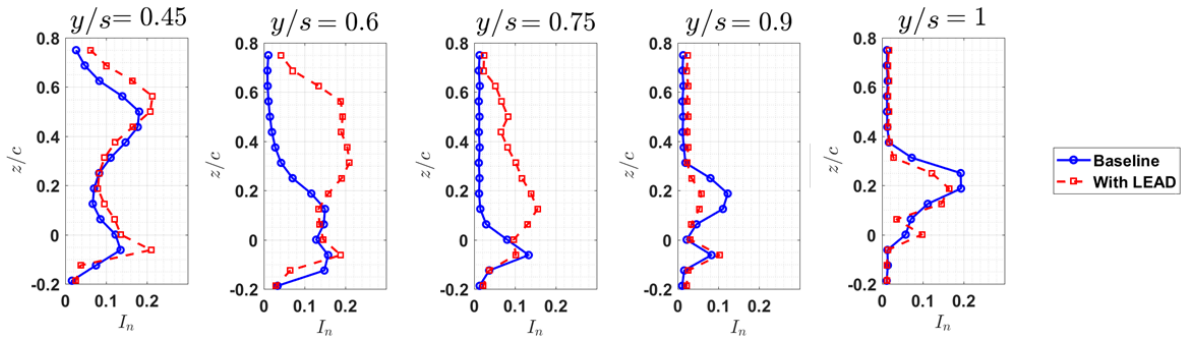

(b) Turbulence Intensity Levels. The velocity fluctuations over time (standard deviation) were evaluated at each spanwise location starting from 0.2c below to 0.8c above the wing upper surface.

Figure 31: Boundary layer sampling results under Post Stall conditions (α = 26°) at Re = 135,000. The LEAD root was fixed at the 60% location. The LEAD parameters were fixed at β = -5° and γ = 22°.

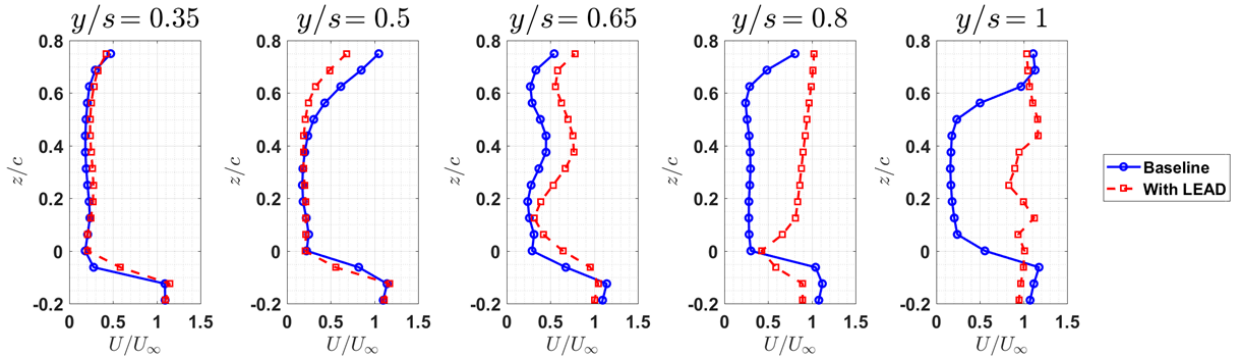

(a) Velocity Deficit Profiles. The mean velocity over time were evaluated and normalized by the freestream velocity at each spanwise location starting from 0.2c below to 0.8c above the wing upper surface.

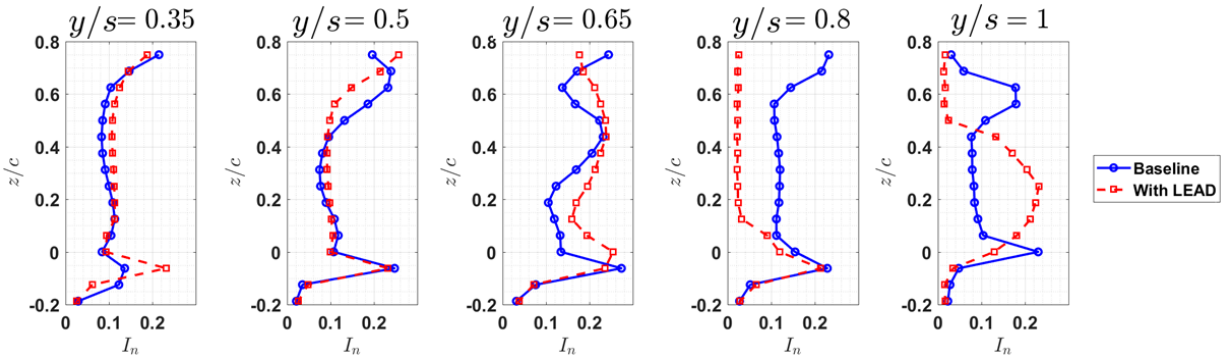

(b) Turbulence Intensity Levels. The velocity fluctuations over time (standard deviation) were evaluated at each spanwise location starting from 0.2c below to 0.8c above the wing upper surface.

Figure 32: Boundary layer sampling results under Deep Stall conditions (α = 34°) at Re = 135,000. The LEAD root was fixed at the 50% location. The LEAD parameters were fixed at β = -13° and γ = 22°.

4.3 Summary of Experimental Results

The results of the force measurements show enhanced lift coefficients of up to 29% at post-stall and 32% at deep stall angles of attack. This validates once again that the LEAD is a post-stall high-lift device. The percent change in lift generated by the rectangular 3D wing equipped with a LEAD, as compared to baseline, was sensitive to the spanwise placement of the device with respect to the wing root. The device also produced higher lift coefficients on a moderate aspect-ratio wing (3D) than it did on an airfoil (2D). These factors prove that the LEAD is a three-dimensional device and its spanwise placement is an important design parameter. The location resulting in the largest improvement was dependent on the angle of attack and the Reynolds numbers. On average, a LEAD placed a 50% spanwise location yielded in the greatest improvements.

These results are enforced through hot-wire anemometry, showing that on a rectangular wing, stall starts from the root and propagates spanwise toward the tip. Inboard of the LEAD root and outboard of its tip, the presence of the device did not significantly alter the flow structure in the wake of the wing. However, the boundary layer near the region of the LEAD mid-span shows a reduction in flow separation in the wake of the base wing. The configurations at Re = 100,000 and the post-stall setup at Re = 135,000 followed this trend. Under deep stall conditions at Re = 135,000, based on the separation observed from root to tip, the entire baseline wing was stalled, and the addition of the LEAD to the wing greatly reduced the velocity deficit in the wake across all locations outboard of the LEAD.

With the LEAD placed at the location of highest lift improvement, the effects of its geometric parameters β and γ were evaluated. Overall, the lower the LEAD relative angle of attack, β, the greater the lift enhancement. This proves that the LEAD stall characteristics are important. Higher tip deflections, γ, also yielded more favorable results in lift improvement. This proves that the size of the gap between the wing upper surface and the LEAD upper surface also plays an important role in the effects of this high-lift device. Lastly, the iso-surface analysis generated a range of values for each geometric parameter that result in percent lift improvements above a desired threshold.

4.4 Discussion

Based on the results obtained, the LEAD is a post-stall lift-enhancing device when placed on the leading edge of a three-dimensional wing of moderate aspect-ratio. For the configurations tested, the device enhanced the post-stall and deep stall lift coefficients.

As the root of the LEAD was moved outboard from the wing root, the percent changes in lift coefficient with respect to the baseline increased. When the device was moved outboard

of the location yielding the highest lift increase, the lift declined to its lowest value once the tip of the LEAD protruded outboard of the wingtip. Since each placement of the LEAD root affected the lift coefficient differently, the three-dimensional effects of the device are important under these flight conditions. On average, the LEAD root placement that yielded the best performance in this experiment was in the middle of the semi-span (50%), which was more outboard of the wing compared to the average alula location on type D avian wings. Since the test specimen was a uniform and rectangular wing, its airfoil distribution across the span did not vary like bird wings (fig 3). In this experiment, the entire wing was more similar to the arm wing, which is the region with thicker airfoils; therefore, the LEAD achieved the highest lift enhancements at a location further outboard than the average alula location in avian wing. Based on the comparison between the three-dimensional and two-dimensional test results, the LEAD generated a higher lift increase on a finite wing than it did on an airfoil confirming that it is a three-dimensional device.

Moreover, the results from hot-wire anemometry have demonstrated that the root of a rectangular wing stalls first, then flow separation propagates outboard along the span. For 3 out of 4 of the configurations tested, root stall was observed, but the velocities in the wake of the baseline wing were fully recovered to freestream along the entire boundary layer near the wing tip. However, in the case of the wing at a deep stall angle of attack at Re = 135,000, a large velocity deficit was observed from root to tip. The addition of the LEAD at the 50% location of the baseline greatly reduced the velocity deficit at all locations outboard of the device. Therefore, the LEAD prevented the wing from fully stalling. These observations also indicate that the LEAD had a greater effect on the flow structure outboard of the device than it did inboard. These results are consistent with the DPIV observations made by Lee et al. [12] that the effects of the alula on the flow were more pronounced on the hand wing than on the arm wing. This behavior suggests that interactions are present between the tip vortex shed by the LEAD and the flow upper surface of the wing, along with the tip vortex shed by the main wing structure.

As far as LEAD geometric parameters are concerned, the results show a range of configurations that caused the most favorable effects in lift generation. The lower the LEAD relative angle of attack, β, the greater the lift enhancement, proving that the LEAD stall characteristics are important. Higher tip deflections, γ, also yielded more favorable results in lift improvement, proving that the gap size of between the wing upper surface and the LEAD tip also plays an important role in the effects of this high-lift device.

Based on the placement and deployment parameters that produced the highest lift enhancement, a small, flexible, and deployable LEAD structure can be developed. Since size and weight are great limitations on UAVs operating at low Reynolds numbers, a well-suited

high lift device need to meet those criteria, as opposed to fixed, large, and heavier slats commonly seen on todays aircrafts. The development of a passively deployable structure calls for further understanding and modeling of low Reynolds number flow around a lifting surface.

5 Concluding Remarks

5.1 Summary of Current Work

In this study consisted of the first efforts to implement a Leading-Edge Alula-Inspired Device on a three-dimensional moderate aspect ratio wing at low Reynolds numbers. To quantify the aerodynamic effects of the device, force measurements were conduted in a wind tunnel to measure the changes in lift generated by a wing with and without the LEAD. Moreover, the boundary layer in the wake of the wing-LEAD assembly was also characterized through hot-wire anemometry.

In general, the results indicate lift-enhancement at post-stall and deep stall angles of attack as well as alleviation of flow separation in the wake of the wing-LEAD assembly. The detailed effects of the device based on flow parameters, wing stall conditions, and LEAD geometric parameters are summarized below as the original research contributions of this work are re-iterated:

- The addition of the LEAD to the rectangular wing produced a decrease in lift when the angle of attack is below α_{STALL}. However, the device increased the lift generated at post-stall and deep stall angles of attack. These results validate once again that the LEAD is a post-stall high-lift device. This is the case when the LEAD is placed on a 3D wing as well as on a 2D wing [**R.C.1**].

- The percent change in lift generated by the rectangular 3D wing equipped with a LEAD, as compared to baseline, was sensitive to the spanwise placement of the device with respect to the wing root. In most cases, the location resulting in the largest improvement was close to middle of the semi-span of the wing (namely 40%, 50%, and 60%). Moving the LEAD inboard or outboard of these ranges results in a lower performance. These factors prove that the three-dimensional effects of the LEAD are important and its spanwise placement along the wing span is an important design parameter. [**R.C.2**].

- At its best location, the lift generated by the 3D wing-LEAD assembly was compared to the results of a 2D setup. The device produced higher lift coefficients on a moderate aspect-ratio wing (3D) than it did on an airfoil (2D), proving that the LEAD is a three-dimensional device [**R.C.3**].

- The effects of the combinations for different geometric parameters were examined. Overall, lower LEAD relative angles of attack, β, and higher tip deflections, γ, yielded the greatest lift enhancement. This proves that the LEAD stall characteristics and

the gap size between the wing upper surface and the LEAD upper surface play an important role in the effects of this high-lift device [**R.C.4**].

- Observations of the flow structure in the wake first confirmed that, on a rectangular test wing, stall forms at the root and propagates spanwise toward the tip. For all cases, the boundary layer at the mid-span location of the LEAD shows a reduction in flow separation in the wake of the base wing. The addition of the LEAD onto a fully stalled baseline wing greatly reduced the velocity deficit at all locations outboard of the device. This proves that the LEAD prevents stall from propagating outboard. This behavior suggests that interactions are present between the tip vortex shed by the LEAD and the flow upper surface of the wing as well as with the tip vortex shed by the main wing structure. [**R.C.5**].

The correlations between aerodynamic performance, flow conditions, and best deployment parameters can be further developed and used to design an adaptive and deployable LEAD that can be implemented on a finite wing to increase mission-adaptability (i.e. expand the flight envelope).

5.2 Recommendations for Future Work

This study evaluated the effects of the geometric parameters of the LEAD on a moderate aspect ratio wing. In the future, additional morphological parameters can be added and evaluated, e.g. the ratio between the LEAD span and the wing span, the LEAD airfoil, the LEAD chord distribution, the angle between the LEAD and wing leading-edges, and more. Additionally, in order to run a finer experiment matrix that takes into account each morphological parameter within a reasonable time period, it is necessary to design a system that automates the change between LEAD configurations without opening the wind tunnel.

Moreover, further experiments are necessary in order to capture the interaction between the two tip vortices shed by the base wing and the LEAD. To fully understand the flow structure around the wing-LEAD assembly, 3D flow visualization techniques can be implemented. Possible methods include particle tracing (e.g. smoke or oil particles) such as 3D PIV, surface flow visualization (e.g. fluorescent oil applied to the wing), and optical methods (e.g. Schlieren photography, shadowgraph, and interferometry).

Once a sufficient understanding of the system through experimental data has been reached, the results obtained can then be used as inputs of an aerodynamic model. One possible method is to develop a discrete vortex model of the aerodynamic behavior of a rectangular wing with a LEAD model added. In the long run, the fluid-structure interactions can also be simulated in an aeroelastic model.

In nature, the alula is an adaptive and flexible high-lift device that is only deployed during maneuvers that demand high maneuverability at steep angles of attack. Therefore, these efforts will eventually lead to the design of an adaptive and deployable device for small-scale UAV wings.

6 References

[1] P. C. Withers, "An aerodynamic analysis of bird wings as fixed aerofoils," vol. 90, no. 1, pp. 143–162.

[2] B. W. McCormick, *Aerodynamics, Aeronautics, and Flight Mechanics*. Wiley, 2 edition ed.

[3] A. Mohamed, K. Massey, S. Watkins, and R. Clothier, "The attitude control of fixed-wing MAVS in turbulent environments," vol. 66, pp. 37–48.

[4] B. Tobalske, "Biomechanics and physiology of gait selection in flying birds," vol. 73, no. 6, pp. 736–750.

[5] J. D. J. Anderson, *Fundamentals of Aerodynamics*. McGraw-Hill Education, 5 ed.

[6] P. B. S. Lissaman, "Low-reynolds-number airfoils," vol. 15, no. 1, pp. 223–239.

[7] J. J. Videlier, *Avian Flight*, vol. 14 of *Oxford Ornithology Series*. Oxford University Press, 1 ed.

[8] B. Austin and A. Anderson, "The alula and its aerodynamic effect on avian flight," in *ASME 2007 International Mechanical Engineering Congress and Exposition*, vol. 7, pp. 797–806, ASME.

[9] O. B. O. Savile, "Adaptive evolution in the avian wing," vol. 11, no. 2, pp. 212–224.

[10] T. Liu, K. Kuykendoll, R. Rhew, and S. Jones, "Avian wing geometry and kinematics," vol. 44, no. 5, pp. 954–963.

[11] S. Podulka, R. W. Rohrbaugh, R. Bonney, and 1954-, *Handbook of bird biology*. Cornell Lab of Ornithology.

[12] S.-i. Lee, J. Kim, H. Park, P. G. Jaboski, and H. Choi, "The function of the alula in avian flight," vol. 5.

[13] J. Meseguer, S. Franchini, I. Prez-Grande, and J. L. Sanz, "On the aerodynamics of leading-edge high-lift devices of avian wings," vol. 219, no. 1, pp. 63–68.

[14] W. Nachtigall and B. Kempf, "Vergleichende untersuchungen zur flugbiologischen funktion des daumenfittichs (alula spuria) bei vgeln," vol. 71, no. 3, pp. 326–341.

[15] J. Alvarez, J. Meseguer, E. Meseguer, and A. Perez, "On the role of the alula in the steady flight of birds," vol. 48, no. 2, pp. 161–173.

[16] A. R. Weyl, "Highlift devices and tailless aeroplanes," vol. 17, no. 10, pp. 292–297.

[17] A. M. O. Smith, "High-lift aerodynamics," vol. 12, no. 6, pp. 501–530.

[18] I. H. Abbott and A. E. V. Doenhoff, *Theory of Wing Sections, Including a Summary of Airfoil Data*. Courier Corporation.

[19] D. Rao and T. Kariya, "Boundary-layer submerged vortex generators for separation control - an exploratory study," in *1st National Fluid Dynamics Conference*, Fluid Dynamics and Co-located Conferences, American Institute of Aeronautics and Astronautics.

[20] M. S. Gen, . Kaynak, and G. D. Lock, "Flow over an aerofoil without and with a leading-edge slat at a transitional reynolds number," vol. 223, no. 3, pp. 217–231.

[21] B. A. Mandadzhiev, M. K. Lynch, L. P. Chamorro, and A. A. Wissa, "An experimental study of an airfoil with a bio-inspired leading edge device at high angles of attack," vol. 26, no. 9, p. 094008.

[22] B. A. Mandadzhiev, M. K. Lynch, L. P. Chamorro, and A. A. Wissa, "Alula-inspired leading edge device for low reynolds number flight," p. V002T06A016.

[23] A. C. Carruthers, S. M. Walker, A. L. R. Thomas, and G. K. Taylor, "Aerodynamics of aerofoil sections measured on a free-flying bird," vol. 224, no. 8, pp. 855–864.

[24] M. Selig, J. Guglielmo, A. Broeren, and P. Giguere, "Summary of low-speed airfoil data."